The Channeling Effect in Ultra-Thin dE-E Monolithic Silicon Telescopes

Fredrik Parnefjord Gustafsson

Thesis submitted for the Master's degree in Physics

Abstract

A new method has been proposed to study the low energy resonances of $^8\text{Li}(\alpha, n)^{11}\text{B}$ at $E_{\text{cm}} \cong 0.5$ MeV using dE-E Monolithic Silicon Telescopes (MSTs). Each telescope consists of five ultra-thin ~ 1 µm (ΔE) silicon detector pads on a ~ 500 µm (E) silicon detector. Both preliminary experiments and simulations show promising results for identifying the reaction cross-section at the low energy. To assure optimal detector performance it is crucial to determine the detector characteristics and response for particles incoming at different angles. Ultra-thin silicon detectors are particularly prone to the channeling effect which degrade the detector signal for incident particles along the crystal planes. A Pelletron tandem accelerator at RIKEN Nishina Center, Japan was used to accelerate ions of ^{11}B, $^{63,65}\text{Cu}$ and ^{197}Au into the MST at different angles and energies. Based on these measurements the optimal detector orientation with minimal channeling could be determined to 10 degrees in between the silicon crystal axis [111] and $\langle 231 \rangle$. Additionally, the detector dead-layers were deduced, indicating a minimum detectable ^{11}B ion energy of 2.4 MeV at the optimal detector orientation.

Contents

CONTENTS

List of acronyms

MST	Monolithic Silicon Telescope
DPP-PHA	Digital Pulse Processing- Pulse Height Analysis
SRIM	The Stopping and Range of Ions in Matter
DAQ	Data acquisition
FWHM	Full width at half maximum
DC	Direct current

Acknowledgments

Firstly, I wish to express my sincere thanks to Jenny Hiu Ching Lee at The University of Hong Kong for making this project possible and for all her precious support. I would also like to give my greatest gratitude to Shunji Nishimura at RIKEN Nishina center as the project supervisor for his valuable guidance provided throughout this project. Furthermore, I am very grateful for working together with my fellow labmate, Dolachay Boniface, who contributed greatly to the success of this work. Additionally, I wish to acknowledge Vi Ho Phong for his extraordinary assistance and contribution as well as staff at RIKEN for their invaluable support. Moreover, I would like to express my greatest thanks to my thesis supervisor Pavel Golubev at Lund University for sharing his expertise and his valuable guidance and also Anton Roth for his great help and supportive comments for this thesis work. Last but not the least, I would like to thank my family for encouraging me throughout this work and in life in general.

Chapter 1

Introduction

The majority of visible matter in our universe is made up of the elementary particles quarks and gluons which together form the nucleons (protons and neutrons). Different combinations of nucleons held together by the strong nuclear force create the atomic nucleus. This is the basis of all known chemical elements. Understanding the origin and evolution of the chemical elements is of central interest for both cosmology and nuclear astrophysics. According to the standard Big Bang model nucleons started fusing together shortly after the quark-gluon plasma condensed into nucleons and later into nuclei of increasing mass number. However, predictions based on this model fail to describe the abundance of elements above mass number A=7 due to the mass gaps at A=5 and 8 [1, 2]. In a potential inhomogenous Big Bang scenario cosmological processes would lead to a strongly inhomogenous baryon density distribution, forming neutron-rich and proton-rich regions in the very early universe [3, 4]. These regions would allow the formation of short-lived nuclei which could bridge the mass gaps, leading the evolution of heavier nuclei. One suggested reaction chain crucial for the primordial nucleosynthesis in the inhomogenous Big Bang follows:

$$^{1}\text{H}(\text{n}, \gamma)^{2}\text{H}(\text{n}, \gamma)^{3}\text{H}(^{2}\text{H}, \text{n})^{4}\text{He}(^{3}\text{H}, \gamma)^{7}\text{Li}(\text{n}, \gamma)^{8}\text{Li}(^{4}\text{He}, \text{n})^{11}\text{B}(\text{n}, \gamma)^{12}\text{B}(\beta^{-})^{12}\text{C}... \quad (1.0.1)$$
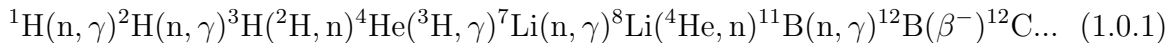
Here consecutive neutron capture events and nuclear reactions lead to an enhanced abundance of ^{12}C and even heavier nuclei [3, 4, 5]. Furthermore, full network calculations indicate that this reaction chain could play a vital role for r-process nucleosynthesis in supernovae [5, 6, 7]. A key channel in this reaction chain is $^{8}\text{Li}(^{4}\text{He}, \text{n})^{11}\text{B}$ due to the short half-life of ^{8}Li of 840 ms [8, 9]. Understanding the cross-section, in the full energy range for the states of ^{11}B, is essential for understanding the conditions constraining this reaction chain. In particular, the low energy reaction cross-section in the Gamow regime $\text{E}_{cm}<2$ MeV is of critical importance due to possible excited levels in ^{12}B which could enhance the reaction rate at low temperatures ($T_9 = 1 - 5\text{K}$) [5, 9]. In recent decades multiple experiments have been performed to determine the cross-section of this particular reaction, using inverse kinematics of ^{8}Li beam on ^{4}He gas targets [5, 9, 8, 7]. These experiments have successfully been able to determine the cross-section for center of mass energies above 1.7 MeV. However, data is scarce and show remarkable discrepancy below this energy. The difficulty arises from distinguishing the low energy ^{11}B reaction products from the elastically scattered ^{8}Li and other background particles. A different experimental approach was proposed at RIKEN, Japan that would allow the low energy cross-section to be determined using ultra-thin dE-E Monolithic Silicon
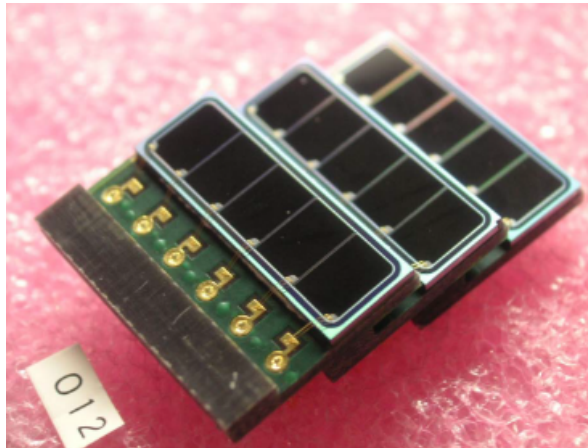
Figure 1.1: The figure shows a set of three individual MSTs. Each MST has an area of 4×15 mm with 5 individual dE detector pads with an area of 3×4 mm.

Telescopes (MSTs) [7]. The MST is composed of five $\sim$1 µm (dE) silicon pads on top of a single $\sim$500 µm (E) silicon detector, see figure 1.1. A detector array with 18 detector pads were tested at CNS Radio Isotope Beam separator (CRIB) in RIKEN, Japan (2005) which showed promising preliminary results for the detection of ^{11}B at the very low center of mass energy $\cong$0.5 MeV [8]. However, before the final experiment can be performed the characteristics of the MST must be investigated.

The MST is capable of both particle identification and energy determination by identifying the particle stopping power. Incident particles deposit some of their energy in the dE detector pad and the remaining energy when stopping in the E detector. The main energy loss is through the ionization of the target material. The electric field created by an external bias forms a depletion region in each detector, charge carriers in this region are separated and collected at the detector nodes. Since the charge is proportional to the energy deposited in the depletion regions the particle stopping power and energy can be determined with the combined information of both dE and E detectors. Each detector has inactive dead-layers; regions where particle energy is undetectable. For accurate particle detection it is essential to understand the size of the dead-layers in both detectors. Furthermore, particles incident on the ultra-thin dE detectors are expressly prone to the channeling effect [10]. Incoming particles incident along the crystal planes or axis can pass through crystal channels with reduced stopping power. Channeled particles will thus result in a reduced signal in the dE detectors. This causes great concern when it comes to accurate particle identification which is crucial for the low energy reaction experiment. Understanding how the channeling effect influences the detector response at various angles is therefore essential for the optimal working conditions of the final detector configuration.

In this thesis the characteristics of the MST is determined through systematical investigation in an in-beam environment using the Pelletron accelerator at RIKEN Nishina center. Ions at different energies and angles of incidence are used to determine both the channeling effect and dead-layer thicknesses, leading to a conclusion of the optimal detector orientation for the final ^{8}Li(^{4}He, n)^{11}B cross-section experiment.

1.1 Objectives

The main objectives for this master's thesis are the following:

- Investigate the MST signal characteristics.

    - Construct a detector setup for digitizing signals from all detector channels.
    - Investigate pulse properties and develop an offline pulse height analysis program for particle identification using an α-source

- Examine the detector signal at different angles of incidence.

    - Build a target vacuum chamber for use at a Pelletron accelerator beamline complete with accurate detector angle control.
    - Operate a Pelletron accelerator using different ion beams on detector target at varying angle of incidence.

- Determine the detector limitations and optimal detector orientation.

    - Develop a general method for quantifying the channeling effect and determine the optimal detector orientation with minimal channeling.
    - Determine the thickness of both dead-layers in the MST using simulations.

1.2 Outline

The thesis will begin with the concept of particle identification using double layered dE-E detectors. This is followed by the underlying principle behind the semiconductor detector and possible problems associated with these types of detectors such as the channeling effect and dead-layers. The specifics of the MST is later introduced combined with a description of the pulse readout using charge sensitive preamplifiers. In chapter 3 the preliminary detector set-up and testing procedure is described. The first detector signal from a ^{241}Am alpha source are displayed and processed using a developed offline pulse trace analysis program to create a dE-E spectrum. In the following chapter 4 the necessary preparations for the accelerator experiment are presented including beamline configuration, noise considerations and beam-target angle calibration. Additionally, considerations regarding ion beams at the accelerator are included. In chapter 5 the methodology for testing the MST characteristics at different angles is described combined with the initial digital data processing procedure. Finally, the results from the experiments are presented and discussed in chapter 6. Optimal detector resolution, detector orientation with minimal channeling combined with an analysis of both dead-layers concludes this work.

Chapter 2

Experimental background

All particle detectors are based on the detection of particle matter interactions. One of the most basic principle of particle detection is through the collection of charge created in particle collisions with the absorber material, such as gas or a semiconductor crystal. Accurate measurement of charge carriers in the absorber material reveal the energy of the particle. However, measuring the charge distribution along the trajectory provides further insight of the type of particle involved in the collision. This can be done Using two or more detectors commonly referred to as a telescope. One type of ultra-thin dE-E monolithic silicon telescope is investigated in this work. In the first two subsections of this chapter the concept of ion matter interaction is described leading to the explanation of how particles can be identified using dE-E telescopes. Secondly, an approach for collecting the charge carriers using semiconductor detectors are thoroughly described starting from section 2.2. The characteristics of these detectors and the relevant problems associated with semiconductor detectors are presented such as the channeling effect and dead-layers which are central to this work. In section 2.3 the details of the MST is provided proceeded by an explanation of the detector signal before and after amplification using charge sensitive preamplifiers.

2.1 Ion matter interaction

Ions can interact with matter through many different processes. The dominating one is through the electromagnetic interaction between ion and the electrons and nuclei in the absorber material. When the ion enters the absorber all nearby electrons and nuclei experience an impulse caused by the electric field of the passing ion. Due to the low mass of the electrons they are more susceptible to the impulse resulting in excitation of the electron orbit or, if the impulse is sufficiently large, escape the atomic potential. The large momentum of the ion means that it will plow through a large quantity of electrons until the energy is no longer sufficient to ionize further. Electrons close to the ion trajectory can gain enough energy to scatter further with surrounding electrons. If the mass of the target nucleus is comparable to the ion mass then a substantial amount of momentum can be lost through direct nuclear recoils. These nuclear recoils can dislocate atoms and damage lattice structures or even generate vibrations (phonons) [21] resulting in non-ionizing energy losses within the absorber material. Furthermore, direct nuclear reactions can occur if the energy is sufficient. These nuclear interactions

are however rare in comparison to the electron scattering. Altogether, the consecutive ion scattering events disperse the energy of the ion leaving a free charge cloud in its path of positive and negative charge carriers. Assuming the ionization potential is much lower than the kinetic energy of the ion, the generated number of charges required to stop the ion will thus be proportional to the ion energy. Accurate measurement of the charge in the absorber material can therefore give insight in the energy and nature of the ion.

The charge distribution along the trajectory depends on the rate of energy loss through the material. The rate of energy loss is defined by the stopping power, $S(E) = -dE/dx$. In most cases the majority is lost through the interaction with the electrons and is often referred to as the electronic stopping power $S_e(E)$ while the energy lost to nuclear recoils is called nuclear stopping power $S_n(E)$. In the early 1950s an expression was first derived by Bethe describing the classical expression for linear total stopping power[11],

$$-\frac{dE}{dx} = \frac{4\pi}{m_e c^2} \cdot \frac{nZ^2}{\beta^2} \cdot \left(\frac{e^2}{4\pi\varepsilon_0}\right)^2 \cdot \left[\ln\left(\frac{2m_e c^2 \beta^2}{I \cdot (1-\beta^2)}\right) - \beta^2\right]. \qquad (2.1.1)$$

This formula describes the amount of energy loss in a material from collisions with electrons in an amorphous material where m_e is the electron mass, Z is the atomic number of the absorber material, v is the ion velocity where $\beta = \frac{v}{c}$ and c the speed of light, n is the electron number density given by $n = \frac{N_A \rho Z \rho}{A M_u}$ where ρ material density, N_A is Avogadro's number, A is the mass of the absorber atom in atomic mass unit, M_u is the mass conversion coefficient and finally I is the mean excitation potential often given by $I = (10 \pm 1) \cdot Z \ eV$. The Bethe expression is in general valid for particles with energy much greater than the bound electron states. Additionally, it does not include radioactive synchrotron losses which are relevant for higher energy relativistic particles. Bloche worked together with Bethe correcting the model to what is known as the Bethe-Bloche equation [11] which more accurately describes the stopping power of particles while taking radiative losses as well as nuclear shell correction into account.

Commonly Monte Carlo computer programs are used to calculate the interactions of ions with amorphous absorber materials. In this work SRIM (The Stopping and Range of Ions in Matter) and in particular TRIM (TRansport of Ions In Matter) will be used to simulate the ion trajectories in different materials. These programs have been extensively tested and verified to accurately predict the ion range in wide range of different materials [19].

2.1.1   The Bragg curve

The specific energy loss for the ion stopping changes with depth into the absorber material. The function of the specific energy loss with respect to the penetration depth is known as the Bragg curve, see figure 2.1. Particles with high energy will experience relatively low stopping power in the absorber, this is due to the short time spent in the vicinity of the electrons results in a low impulse. When the particle slows down in the material, impulse increases resulting in greater ionization up to a maximum called the Bragg peak as seen in the figure 2.1.

The rate of energy loss determines the range into the material. The ion range is a statistical quantity which depends on the multiple scattering events occurring in the
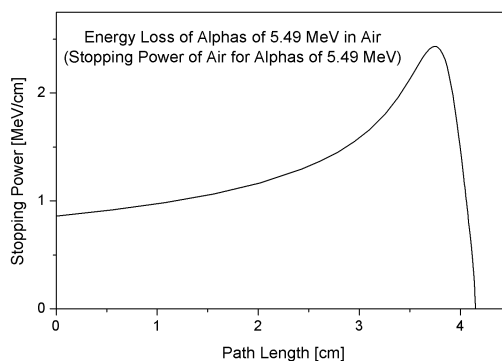
Figure 2.1: Stopping power of alpha particles as a function of path length in air. The Bragg peak with maximum stopping power can be seen near the end of the particle trajectory.

absorber. The amount of dispersion along the particle trajectory is called straggling which in turn determine the range distribution in the material.

2.1.2   dE-E particle identification

Most particle detectors capture the generated charge in the detector material in order to determine the particle energy. However, if both energy and the particle stopping power can be determined then the type of particle involved in the collision can be identified. Looking back at the Bethe equation 2.1.1 for low energy ions $v << c$ (which is generally valid for the ions of interest in this experiment) then the equation can be simplified to;

$$-\frac{dE}{dx} = \frac{4\pi n Z^2}{m_e v^2} \cdot \left(\frac{e^2}{4\pi\varepsilon_0} \right)^2 \cdot \left[\ln \left(\frac{2m_e v^2}{I} \right) \right].$$

If we rewrite the expression in terms of the non-relativistic kinetic energy for the ion $E = \frac{mv^2}{2}$ where m is the ion mass, then the expression becomes,

$$-\frac{dE}{dx} = \frac{2\pi n Z^2 m}{m_e E} \cdot \left(\frac{e^2}{4\pi\varepsilon_0} \right)^2 \cdot \left[\ln \left(\frac{4m_e E}{Im} \right) \right].$$

This simplified expression describes how the particle stopping power varies with ion energy E, charge Z and mass m assuming amorphous detector material. In figure 2.10 the simplified stopping power function for the three particles relevant to the experiment have been plotted ^{11}B, ^{8}Li and ^{4}He [11]. Due to the approximations the plotted functions fail to describe the low energy regime accurately.

In order to determine the stopping power function experimentally, double layered detector are used with a thin dE/dx detector commonly referred to as a dE detector in front of a larger E detector in a telescope configuration. Particles with sufficient energy will pass through the thin dE detector resulting in a signal corresponding to the energy loss in the detector thickness dx. The particle is then stopped in the larger E detector which captures the remaining ion energy, see figure 2.2a. Ions with a specific charge-mass-energy ratio entering this detector will thus provide a coordinate in the dE/dx-E plot creating a 2D particle identification spectrum. Recorded coincidence events from a specific particle will register as events along the stopping power function
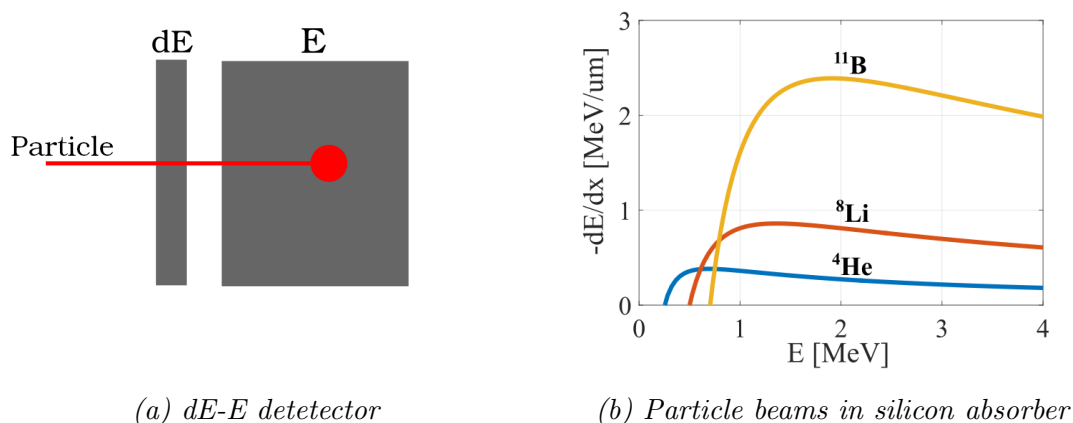
(a) dE-E detetector   (b) Particle beams in silicon absorber

Figure 2.2: Particle energy loss (dE/dx) as a function of energy (E) in a silicon absorbed can be seen in figure (b) which represents the signals from a dE-E detector (a).

which can be used for particle identification purposes. This simple concept allows for relatively accurate particle identification which is the concept of the ultra-thin dE-E MST investigated in this thesis.

2.2   Semiconductor detectors

Essential for particle detection is the collection of charge carriers in the detector, semiconductors are highly regarded for this purpose. Semiconductors such as silicon or germanium have crystalline structure with half filled outer atomic shells. The periodicity of the crystalline structure forms band structures with closely spaced energy levels. The spacing between the outermost conduction band and the valence band is called the band gap, see figure 2.3.
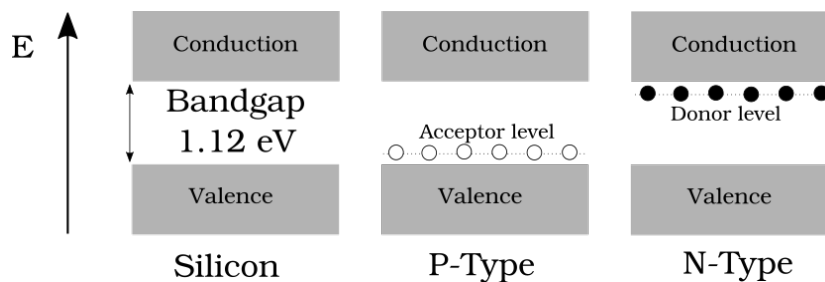

Figure 2.3: The figure displays the silicon band-gap for pure silicon, N-type silicon and P-type silicon.

Materials lacking band gaps allow free movement of electrons in the conduction band and are called conductors. Insulators have a large energy gap of about 5 eV requiring a large energy to excite electrons into the conduction band, explaining their high resistance. In a semiconductors the band-gap is small, usually in the order of 1 eV. When sufficient energy is provided to an electron in the lattice it can be excited into the conduction band leaving a vacancy in the valence band called a hole. Due to the small band-gap a large quantity of charge carriers, both holes and electrons, are generated

along the ion trajectory. The large number of charge carriers result in large statistics when determining the energy loss in the absorber. Additionally, semiconductor materials usually have a high mobility for these charge carriers at room temperature. This combined with a relatively high electron density makes semiconductors good candidates for particle detection.

In order to collect the free charge carriers in the semiconductor an electric field is required to separate the holes from the electrons and therefore reduce recombination. Unlike gas detectors an intrinsic electric field can be generated through slight modifications in the band-gap structure by introducing impurities in the lattice. If an atom with a single electron in its valence level is introduced in the lattice it will generate a donor level slightly below the conduction band. The extra electron is loosely bound and thermal excitation can easily dislodge the electron from the donor level filling the conduction band. Examples of such n-type impurities are lithium, arsenic and antimony which can be are introduced in low concentration ($10^{10} \mathrm{cm}^{-3}$) in the crystal through sputtering or ion implantation [11]. If the semiconductor is instead doped with atoms lacking a covalent bond with an electron vacancy in its outer shell, an acceptor level can be created slightly above the valence band, see figure 2.3. Likewise, thermal excitation can fill the vacancy with an electron from the valence band. This usually occurs when the semiconductor is doped with boron, aluminum or gallium, this doping is called p-type. When the two different types of doped semiconductors are brought together, the electrons in the conduction band will tend to recombine with the holes in the valence band forming a p-n junction, see figure 2.4. This so called diffusion current is quickly counteracted by the increasing electric field generated from the charge separation generating a drift current in the opposing direction. The p-n junction at equilibrium has a steady state charge separation with a built-in potential given by,

$$V_0 = \frac{K_b T}{e} \ln \frac{N_d N_a}{n_i^2} \tag{2.2.2}$$

where K_b is Boltzmanns constant, T is the temperature, e is the unit charge, N_d is the donor concentration, N_a is the acceptor concentration and N_i is the intrinsic concentration of the substrate. The size of the depletion is in turn described with,

$$d = \sqrt{\frac{\epsilon V_0}{e N}}. \tag{2.2.3}$$

Where N is the dopant concentration of the type with lowest concentration (either N_a or N_d). Due to the direction of the electric field in the depletion region electrons encounter higher resistance traveling against the direction "reverse" of the electric field and lower resistance when traveling along the electric field "forward". This is the concept of the rectifying diode. When an ionizing particle pass the depletion region the electrons and holes will be created and drift to either end of the p-n junction where they will be collected. Charge carrier creation occurring outside the active depletion region will recombine and therefore not be collected. The low intrinsic electric field of about 1 V is often insufficient to completely separate the charge carriers fast enough before recombination occur within the depletion region. A large amount of the signal is therefore lost, resulting in poor energy resolution and efficiency. Assuring optimal charge collection an external reverse bias voltage V is applied over the p-n junction
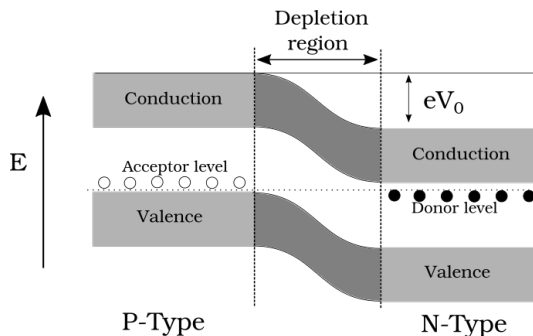
Figure 2.4: Overview of a p-n junction with built in potential V_0.

which increases the potential difference in the depletion region. The depletion therefore increases accordingly,

$$d = \sqrt{\frac{\epsilon(V_0 + V)}{eN}} \tag{2.2.4}$$

Higher bias voltage and lower impurity concentration increases the detector volume which is necessary for an efficient detector. Regions outside this depletion region are called dead-layers which are described in a later section. As a consequence of the electric field in the depletion region the p-n junction will acquire a capacitance which is often a cause for concern when it comes to the particle detection due to the increased sensitivity to external noise discussed in section 2.3.1.

2.2.1 Silicon diode detectors

The first type of semiconductor detector was based on silicon crystals. Unlike the semiconductor germanium detectors, which is commonly used for gamma spectroscopy, silicon detectors do not require cooling due to the larger band-gap of 1.12 eV. However, the larger band-gap results in smaller number of free charge carriers, the lower statistics per event decreases the energy resolution. Many different types of silicon detectors exist today which are commonly used in nuclear and particle physics experiments. Examples are silicon in the silicon drift detectors and silicon strip detectors. A typical silicon drift detectors utilize a single long connector cathode or anode on top of a doped silicon wafer. The position of the particle event can be determined from the time it takes for the captured charge to travel to the detector readout node given the detector geometry. In the silicon strip detector regions of doped silicon are arranged in a matrix or arrays on a larger silicon wafer where each doped region function as a separate detector. The MST is a type of double-layered silicon strip detector.

2.2.2 Dead-layer

The inactive regions of the detector outside the depletion region are called dead-layers. Electron and hole pairs formed will simply recombine since no electric field can pull them towards the detector readout nodes. Therefore, all energy deposited in these regions are lost for detection. The dead-layer size in the detector can be minimized by fully depleting the detector by increasing the bias voltage. However, reducing the

dead-layer is technically challenging. Usually a thin metal film is placed on the surface of silicon detectors to prevent damage and oxidation during handling [12]. Thin dead-layers are relevant when detecting low energy ions with large stopping power since a significant amount of the particle energy can be lost. There are many approaches to determine the thickness of the dead-layers, one common approach is using a defined ion beam at varying angle of incidence as seen in figure 2.5. Assuming ions of known energy E_{ion} are incident on a detector with a dead-layer then,

$$E_{tot} = E_{det} + E_{dl}$$

Where E_{det} is the energy detected in the active detector region and E_{dl} is the energy lost in the dead-layer. Assuming that the ion is incident at an angle θ to the detector normal and the detector signal x_{det} is proportional to the energy with a calibration gain constant G_{det}. Then the above expression with energy lost in the dead-layer at 0 degree incidence E_{dl0} can be rewritten as,

$$E_{tot} = G_{det} x_{det} + \frac{E_{dl0}}{\cos(\theta)}.$$

This expression can be restructured in terms of the detector signal,

$$x_{det} = -\frac{E_{dl0}}{G_{det}} \left(\frac{1}{\cos(\theta)} \right) + \frac{E_{tot}}{G_{det}}. \tag{2.2.5}$$

Assuming that the stopping power is constant around the region close to the border between the dead-layer and detector then it can be used to determine both detector gain and energy lost in the dead-layer, knowing the ion energy and angular dependence of the detector signal. The equivalent dead-layer thickness in terms of silicon can be determined if the energy lost in the dead-layer is known.
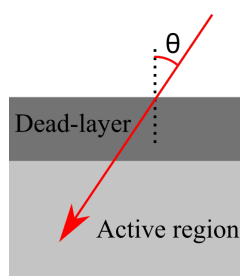

Figure 2.5: Particle incident on a detector with dead-layer.

2.2.3 The plasma effect

When a heavy ion with large stopping power enters the detector a high density of charge carriers is created over limited detector volume. If the electric field is insufficient to quickly separate the charge carriers then recombination will occur before the charge carriers have been collected by the readout electronics. The retarded collection time is commonly denoted the plasma time, which is the time it takes for the plasma to disperse before charges can be collected [14]. This effect results in a drastically reduced signal for strongly ionizing events which consequently leads to a reduced detector resolution.

It is therefore essential to have a sufficient electric field within the depletion regions to prevent the plasma effect.

2.2.4 Silicon crystal structure

All mono-crystalline structures are based on primitive unit cells which are repeated forming the bulk crystal. The unit cell defines the shape and symmetry of the complete crystal lattice. Silicon detectors are based on a mono-crystalline silicon with a face center cubic unit cell configuration similar to diamond, see figure 2.6. The unit cell is denoted with the lattice parameters **a**,**b** and **c** which are vectors of equal length of 5.43Å for the orthogonal silicon crystal. The orientation of the crystal lattice is
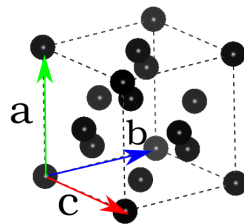

Figure 2.6: A single unit cell of FCC silicon crystal.

typically denoted using the miller indices h,k and ℓ. These indices describe the crystal plane intercepting the points $\mathbf{a}/h$,$\mathbf{b}/k$ and $\mathbf{c}/\ell$ in the crystal lattice where the plane is referred to as $(hk\ell)$. Examples of miller indices of the major crystal planes can be seen in figure 2.7. The crystal direction is for a cubic cell represented by the surface normal to the crystal planes denoted using $[hk\ell]$.
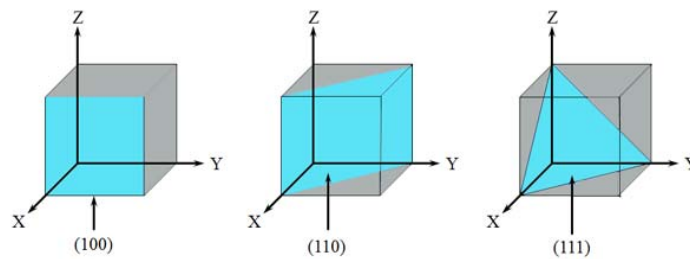

Figure 2.7: Examples of crystal planes represented by the colored planes with corresponding miller index.

2.2.5 The channeling effect

The stopping power for particles incident on crystalline materials are significantly reduced at particular angles along the crystalline axis. This is called the channeling effect. Particles incident along a crystal axis will experience small angle scattering guiding the particle along the crystal channel, see figure 2.8. The lower electron density in the channel means the ion experience a greatly reduced stopping power and can thus travel

deeper into the target material. This is a limitation to the Bethe formula which assumes amorphous target material with no angular dependence. The channeling has been extensively studied by Gemmel [10] who described the critical angle necessary for channeling to occur;

$$\Theta_C = \frac{\sqrt{zZa_0Ad}}{1670\beta\sqrt{\gamma}} \tag{2.2.6}$$

most variables have been defined in equation 2.8 except a_0 which is the Bohr radius, d the spacing between atoms in the channel and γ given by $1/\sqrt{1-\beta^2}$. The critical channeling angle decreases with increased energy but is typically rather small, around 1 degree for ions β =0.1 [11]. The channeling effect is highly dependent on the crystal orientation. Likewise, the phenomena is closely related to similar phenomena dependent on crystal orientation, such as electron backscatter diffraction resulting in Kikuchi patterns, which both give indication of the dominant crystal orientation where channeling can occur, further information regarding these patterns can be found in the reference [15]. In essence, the Kikuchi lines represents the crystal planes while the intersections represent the dominant crystal axis. These pattern provide an orientation map of the crystal, examples of these Kikuchi patterns with corresponding crystal orientation are seen in figure 2.9[1]. Ultra-thin detectors are particularly prone to the channeling effect.
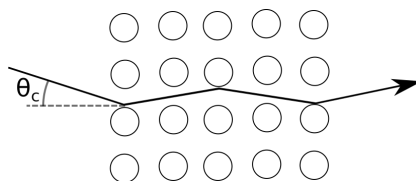

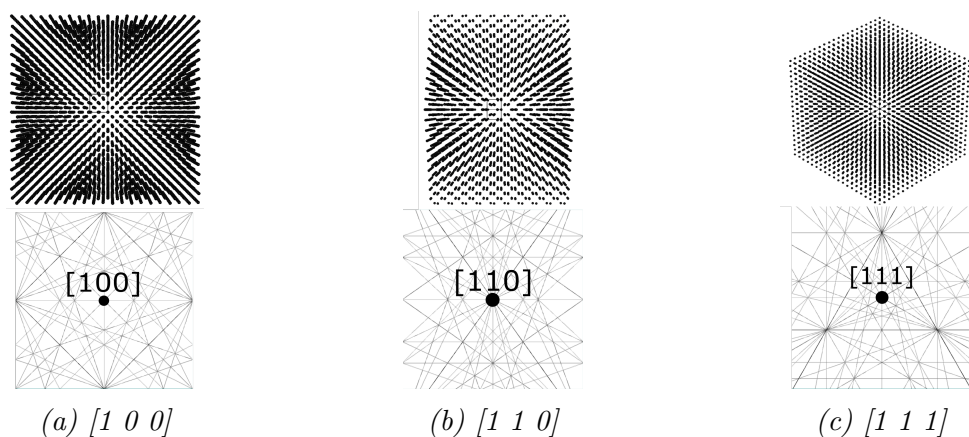Figure 2.8: Particle channeling through a crystal lattice.

(a) [1 0 0]   (b) [1 1 0]   (c) [1 1 1]

Figure 2.9: Silicon crystal viewed along the directions [1 0 0], [1 1 0] and [1 1 1] with associated Kikuchi patterns.[15]

The shorter the channel the higher the probability of the particle successfully channeling through the detector. The main crystal axis corresponding to the intersections in the Kikuchi patterns should be avoided to reduce particle channeling.

---

[1]These simulations were performed using VESTA 3D visualization program [23] combined with Kossel/Kikuchi K-Pattern Simulator [24]

2.3 The dE-E monolithic silicon telescope

The construction of ultra-thin silicon detectors have been made possible in recent decades due to the rapid development of semiconductor technology. In this work a modern type of double layered monolithic silicon telescope (MST) is investigated. The telescope consist of five (3×4 mm) ≈ 1 µm thick dE pads on top of a ≈ 500 µm E detector with a total detector area of (15×4 mm) intended for dE-E particle identification. Two MSTs with a total of 10 dE detector pads are mounted on a 14 pin board as seen in figure 2.10a with a cross-sectional view in figure 2.10b.
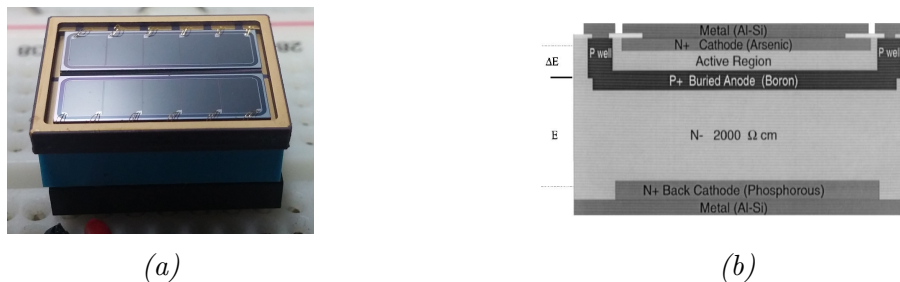

Figure 2.10: Figure (a) shows a a picture of the investigated MST combined with a cross-section of the MST seen in figure (b) [13].

The detector telescope is developed by INFN-LNS, INFN Sezione di Catania and ST-Microelectronics [12]. The telescope is based on High resistivity $2000~\Omega cm$ n-doped silicon wafer with a thickness of around ≈ 510 µm. A p-doped well is formed through treatment with low energy boron implantation followed by high temperature (1050C) diffusion up to 2 µm depth. This is later proceeded by high energy boron implantation forming the buried anode acting as a common ground for both dE and E detector. In order to create the p-n junction for the dE detector pads the surface is n-doped using arsenic. A thin metal film acts as a protective layer on top of the detector surface which is part of the first detector dead-layer. The MST can be connected on the back using a seven pin connector with one ground connection together with one output for the large E layer and five output pins for the dE pads.

Ultra-thin detectors are limited in size due to the high capacitance. During the development the decision was made to separate the dE pads to reduce the capacitance to maximum 1 nF while still keeping a large surface area with five individual pads per telescope[12]. This allows for use without internal preamplifiers.

2.3.1 Detector signal

Figure 2.11 shows the MST internals of one dE detector pad with the E detector. Each detector is represented within the the gray boxes containing a p-n junction symbolized with a diode and internal impedance from its capacitance and internal resistance. All detectors in the telescope are connected to a common ground between the dE pads and E detector. A positive reverse bias voltage below 10 V is applied across the dE detector pads to increase the depletion region. The larger E detector is powered separately requiring a bias voltage around 100 V.

The internal resistance of the detectors prevent greater bias due to the increased leakage current resulting in greater detector noise or even breakdown. Charges are
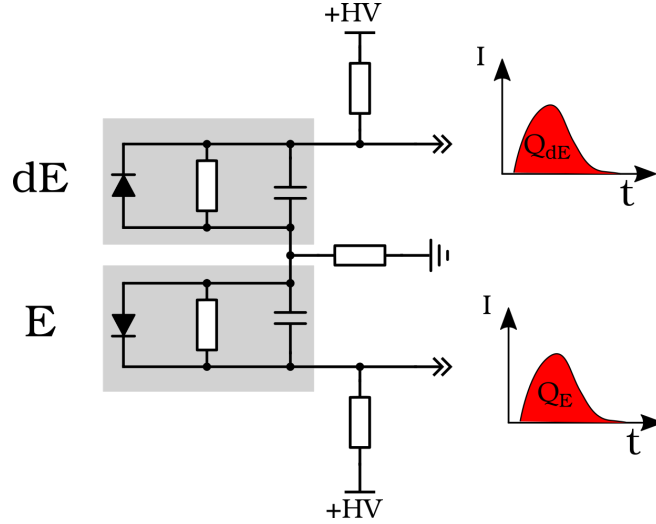
Figure 2.11: Circuit diagram of the MST with dE detector pad and the E detector including the internal capacitance and resistance for both detectors.

separated in the depletion region when an ionizing particle hits the detector. The charge collection time or pulse current generated by this event is directly dependent on the internal detector capacitance. A large detector capacitance reduces the peak current generated from an event and in doing so reduces the signal to noise ratio which is why thin detectors with high capacitance are highly sensitive to noise. The energy deposited in each detector is proportional to the charge (Q_{dE} and Q_E) of the integrated current pulse from the output nodes as seen in figure 2.11. Due to the common ground large current pulses can result in charge accumulation in the common ground between adjacent detectors resulting in overshoot in the smaller dE detector pads [16].

2.3.2   Charge integration using preamplifier

The current pulse generated by the detectors are often difficult to detect, charge sensitive preamplifiers are used in order to both amplify and integrate the signal from the detector. The basic schematics of the charge sensitive preamplifier is seen in figure 2.12. When the current pulse from the detector enters the preamplifier it first passes a AC coupling filter capacitor which allows the short current pulse (usually below a microsecond) to pass while removing the high detector bias voltage. The current pulse from the detector feeds the feedback capacitor C_f with charge Q and in doing so increases its potential given by;

$$V = \frac{Q}{C_f}.$$

A feedback resistor R_f discharges the capacitor with a exponential decay-time τ for the resulting voltage pulse;

$$\tau = R_f C_f.$$

A long decay-time with respect to the rate of the incoming pulses can result in pile-up leading to detector signal saturation. The potential difference in the feedback circuit is then amplified using an operational amplifier with high gain G which increases the output signal to $V_h = G \cdot V$. The feedback circuit is usually configured for the input
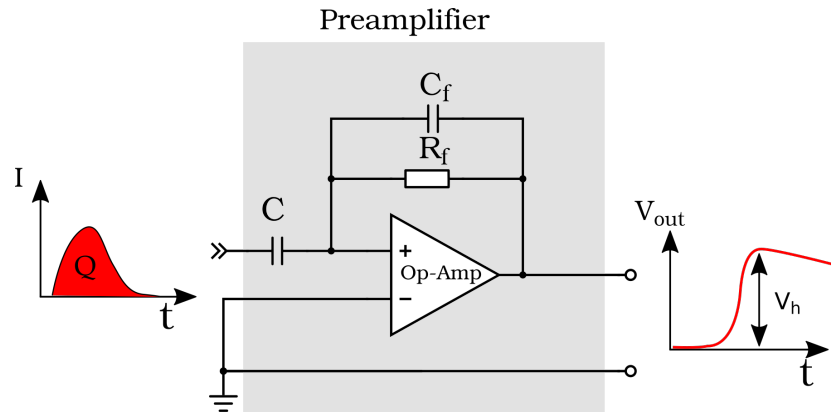
Figure 2.12: Preamplifier schematic with current pulse signal with charge Q amplified creating an output pulse with amplitude V_h.

impedance to assure optimal signal to noise ratio. Additionally, the feedback capacitance should be kept low in comparison to the generated charge to increase the gain of the amplifier a low feedback capacitance does however increase noise sensitivity. The preamplifier is therefore highly susceptible to electromagnetic waves captured by cabling and microphonics and is often kept isolated with a grounded Faraday cage.

2.3.3 Pulse shaping and data acquisition

The peak height of the preamplifier pulse usually linearly correspond to the charge from the detector which in turn is related to the energy deposited in the detector. Due to the high amplification factor the signal can be interpreted using common instruments such as oscilloscopes but are often amplified using shaping amplifiers. These shaping amplifiers use a differentiator and pole-zero cancellation circuit to reduce the decay-time significantly. This allows for higher counting rate before pile-up occurs. Additionally, the amplifier shapes the signal into a Semi-Gaussian which improves the signal to noise ratio with the help from an active integrator. The pulse can then be amplified from a few hundreds of millivolts to a signal of a few volts amplitude, more information is found in [11].

Modern fast digital acquisition units (DAQ) can trigger on the preamplifier pulses. These instruments convert the analog pulse to digital trace by measuring the voltage samples at regular intervals up to gigahertz sample frequency. The digital samples create a trace containing the pulse which can be captured and saved for offline analysis. The signal can also be directly processed online during data acquisition to determine relevant information contained within each pulse.

Chapter 3

Set-up and preliminary detector testing

Preliminary detector preparations and testing was necessary before in-beam measurements. In this chapter the detector setup including signal readout system is presented and discussed. This is followed by the first observed detector signal from alpha particles using an ^{241}Am calibration source. The detector signal characteristics are investigated and a offline pulse height analysis program is developed to process the digitized pulse traces to create dE-E identification spectra. Since only one calibration source was available air attenuation was used to change the energy of the alpha particles entering the detector.

3.1   Detector setup

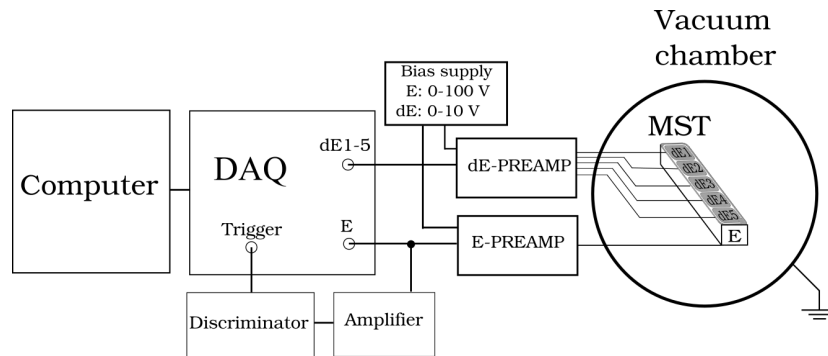The MST was tested using the setup seen in figure 3.1.

Figure 3.1: Setup used to capture signals from the MST.

The MST was mounted on a breadboard with seven pins, six coaxial connectors connected to five dE-pads and a single E detector with one of the pins assigned for the common ground. To assure a noise free testing environment the detector was placed in a stainless steel vacuum chamber with coaxial feedthrough ports allowing the preamplifiers to be placed outside the chamber. The vacuum chamber was connected to a scroll pump capable of reaching a pressure below a few millibars. The detector outputs from the dE and E detector channels were connected to two separate 10 channel

preamplifiers with an interchangeable feedback circuit. Due to the different bias voltage needed of the larger E detector a single preamplifier array could not be used for all detectors. A 4-channel MHV-4 400 V bias power supply was used for applying +0-10 V bias to the dE-preamplifier which in turn is connected to dE-detector pads. A second channel from the bias supply supplied +0-100 V for the larger E-detector through the E-preamplifier. Due to ground loops resulting in noise both preamplifiers were directly screwed to the grounded vacuum chamber enclosing the detector, see figure 3.2. Different feedback circuits were tested to find the optimal signal to noise ratio. A feedback circuit with 4 pF and 1 MΩ was selected for both preamplifiers.
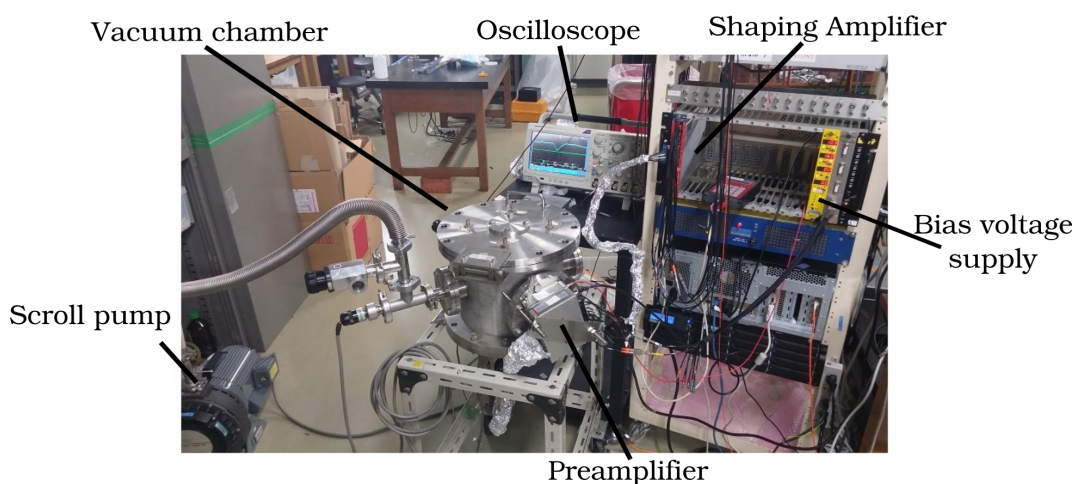

Figure 3.2: Picture of the setup used to test the MST. The detector is placed inside the vacuum chamber and the preamlifiers are firmly attached to the side of the vacuum chamber.

The signals from the dE and E preamplifier output was connected to a 16 ch 14 bit CAEN 1730B DAQ with a sampling speed of 500 MS/s. The E preamplifier output was also connected to a CAEN N568B shaping amplifier together with a discriminator which generated a trigger pulse on the leading edge of the amplified pulse from the E-detector. This was used as a trigger for the DAQ which saves pulses with 2000 samples per trace for all detector channels. The data was then saved in a computer for offline pulse trace analysis.

3.2 Detector testing using ^{241}Am alpha source

Radioactive alpha emitters are commonly used as calibration sources for particle detectors. One such source is ^{241}Am with a half-life of 432 years decaying accordingly,

$$^{241}_{95}\text{Am} \xrightarrow{432.2\text{y}} {}^{237}_{93}\text{Np} + {}^{4}_{2}\text{He}^{2+} + \gamma\ 59.5409 \text{ keV}.$$
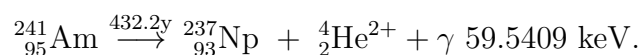
The helium nucleus (commonly referred to as alpha particle) released in this decay has an energy of 5.486, 5.443 and 5.388 MeV with branching ratios 85%, 13% and 2% respectively, accompanied with a low energy gamma photon near 60 keV. A 5 kBq ^{241}Am source was used in these experiment to test the detector response. The source was placed at a distance of 3.5 cm facing the detector within the vacuum chamber.

After applying a bias of 5 V to the dE detector and 100 V to the E detector pulses could be observed from the preamplifier outputs. The rise-time was measured for the dE detectors which varied from 300 to 500 ns with a 5 us decay time while the rise-time for the E detector pulse was measured to around 70 ns with 7 us decay time. When the chamber was evacuated a negative pulse overshoot could be observed in the dE detector signal, see figure 3.3. The overshoot signal seemed to be correlated with the pulse from the E detector affecting adjacent detectors near the event. This overshoot is caused by
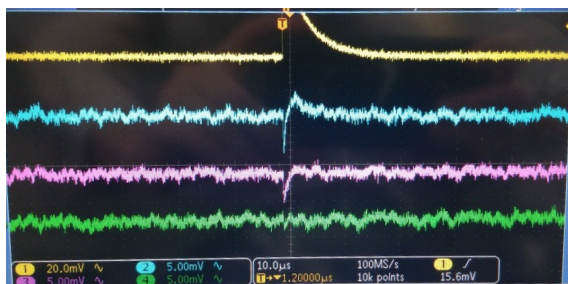

Figure 3.3: Preamplifier signals viewed from oscilloscope; the yellow pulse correspond to the E detector while the other channels correspond to dE2, dE3 and dE4 from above. Pulse overshoot can be seen in dE2 and dE3.

cross-talk between the detectors and is a well known phenomena [16]. This overshoot occur when the common ground in figure 2.11 does not have time to dissipate the charge generated in the E detector. This results in a reverse negative potential across the nearby dE pads. A proposed solution for this cross-talk is to use shaping amplifier with a long shaping time. Since the cross-talk has a short period of a few nanoseconds it has little influence to the much more prominent real detector signal.

3.2.1   Pulse height analysis

When increasing the pressure in the vacuum chamber the amplitude of the E signal decreased while the dE signal increased with a strongly reduced overshoot. This was due to the Bragg peak moving closer to the detector surface inducing a stronger ionization in the dE detector. In order to digitize the data the DAQ was used which was triggered by the discriminator signal see figure 3.4.
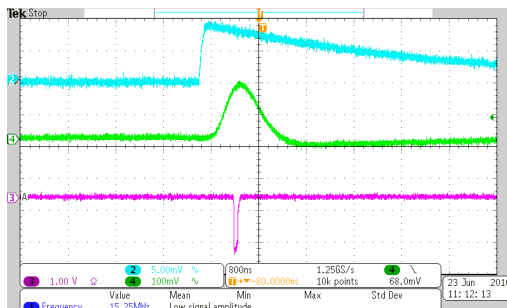

Figure 3.4: The light blue signal correspond to the pulse from the E detector after the pream-plifier, the green is the signal after shaping amplifier and the purple correspond to the trigger pulse from discriminator.

In this configuration pulse traces from all channels in a triggered event were captured with the digitizer as seen in figure 3.5a. The baseline has been set to zero for all channels to compensate for any DC offset. In the offline analysis coincidence events in both dE and E detector were identified by defining a signal threshold for the dE channels. High frequency noise was then reduced through moving-average convolution with a window of 200 data points, see figure 6.1b. The peak height with respect to the baseline was determined from the largest value of the convoluted pulse for both dE and E detector for each event. The detector was exposed to the alpha particles over a time period
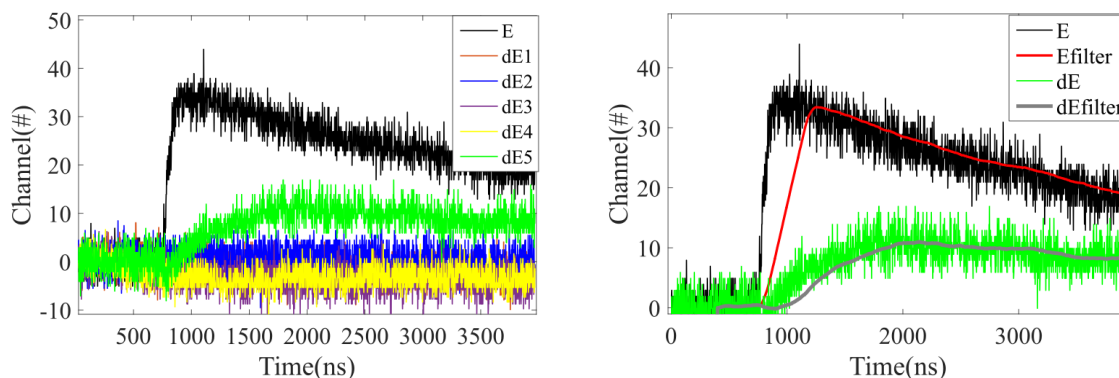
(a) Preamplifier signals after baseline correction.

(b) Coincidence event after moving-average convolution.

Figure 3.5: Captured pulse traces from ^{241}Am alpha particles.

of 1 hour with a count rate of about 1 Hz. The peak height values from both dE and E were ordered in bins of varying value such that a histograms could be created for both detectors. The resolution, commonly defined as the peak position divided by the FWHM of the peak, was determined for both detectors which was 2% for the E detector and 28% for the dE3 detector, see figure 3.6a. A 2D dE-E particle identification spectra could be created from this data as described in section 2.1.2, seen in figure 3.6b.
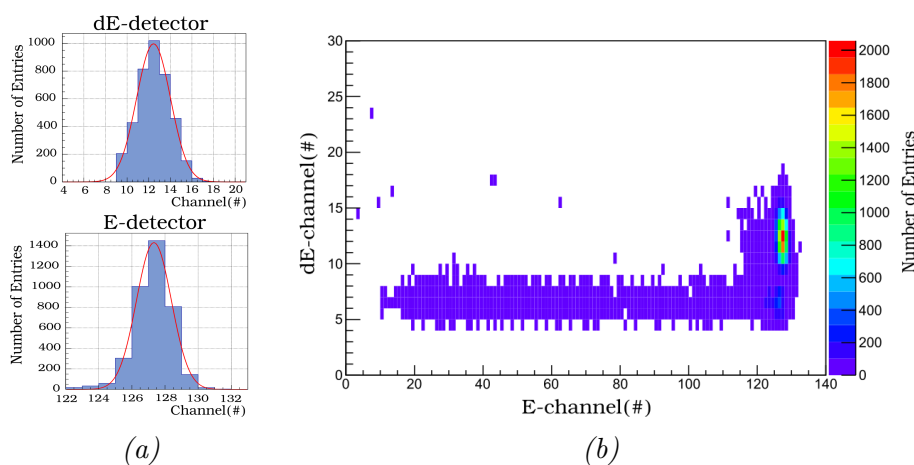

(a)

(b)

Figure 3.6: Figure (a) displays the histogram for dE and E fitted with a gaussian functions with determined resolution (b) shows the particle identification spectra for alpha particles from ^{241}Am in vacuum.

Despite the low signal to noise ratio for the dE detector the alpha particles can easily be identified in this histogram. The low trigger threshold resulted in a band of noise below the real signal.

3.2.2 Alpha particle detection at varying energy

Since no other calibration source was available the detector was tested with the alpha particles attenuated by air at different pressures. The pressure inside the vacuum chamber could easily be adjusted changing the density of air molecules in between the source and detector. Experiments were done at the varying pressure from 0,250, 400, 500, 600, 700, 800 and 900, 1000 mbar with the source 3.5 cm from the detector. The normalized histogram data can be seen in figure 3.7.
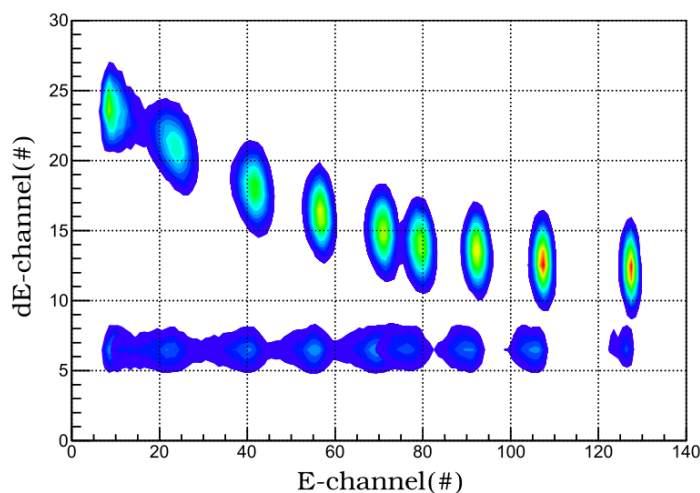

Figure 3.7: Particle identification spectra for alpha particles from ^{241}Am attenuated with 3.5 cm air at different air pressure from 0, 250, 400, 500, 600, 700, 800, 900 and 1000 mbar. The spectrum has been normalized for simplified comparison.

The particle energy decreases with increasing pressure resulting in a lower signal in the E detector. When the particle energy is decreased the Bragg peak moves closer to the dE detector resulting in a greater dE signal. The dE-E identification spectrum can be compared with the theoretical plot seen in section 2.1.2. The lowest detectable alpha particle energy could be determined using Monte Carlo simulations using SRIM. Assuming attenuation by by 3.5 cm air at 1000 mbar the lowest detectable alpha energy could be determined to about 2 MeV. This experiment verifies that the detector has sufficient capability of identifying low energy ions.

Chapter 4

The Pelletron Experiments

The detector had previously been tested using an ^{241}Am calibration source at different energies. However, due to the low count-rate and large divergence the source could not be used to accurately investigate the angular dependence of the MST. A source of collimated monochromatic ions was required. A Pelletron particle accelerator at RIKEN, Nishina center was chosen for this purpose. The Pelletron accelerator is capable of accelerating a large variety of ions up to several MeV with a highly collimated ion beam and a few millimeter beam diameter. Details regarding this accelerator can be found in appendix A. In order to accurately investigate the beam-detector angle a remote controlled rotation-stage was used and calibrated. The beamline configurations and preparations for the in-beam experiments are presented including vacuum considerations and detector noise precautions. This is followed by a section with a motivation of selected ion beams used at the accelerator beamline. The chapter is concluded with an overview of the data acquisition setup.

4.1 Laser detector angle calibration

Accurate beam to detector angle control is essential to investigate the channeling effect and dead-layers in the MST. A motorized rotation-stage was used allowing precise (0.25 degree) remote control of the detector angle inside the vacuum chamber. Before installation a systematic calibration was performed by constructing a laser setup (figure 4.1). This calibration was needed to assure proper alignment of the central dE pad with respect to the rotation axis. To prevent damage of the MST the laser was attenuated using optical filters before reflecting on two mirrors. Using the mirrors the laser beam was directed through two collimators before illuminating one of the dE pads on the MST. The beam projection and reflected laser beam were observed while incrementally changing the detector angle. The detector position was adjusted to make sure the central dE3 pad was illuminated during rotation. The reflected beam angle was observed to verify the accurate angular control of the rotation-stage.

4.2 Beamline configuration

One beamline at Nishina center tandem Pelletron accelerator was used for the experiments. The chamber seen in picture 3.1 which was configured for detector testing was
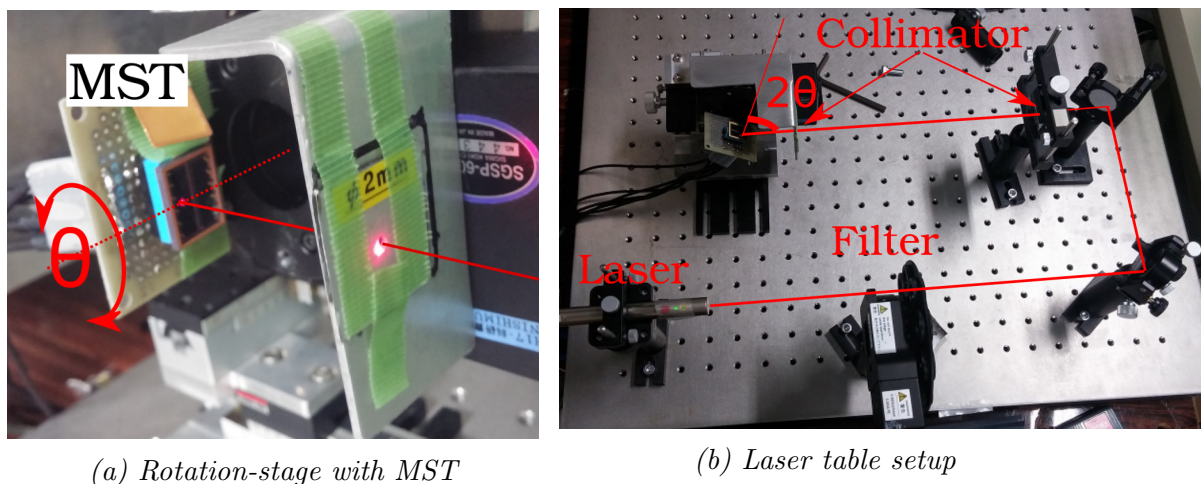
(a) Rotation-stage with MST

(b) Laser table setup

Figure 4.1: Setup used to calibrate the MST to beam angle using a laser setup using rotation-stage.

modified to withstand a vacuum pressure of 10^{-7} mbar required for use at the beamline. A turbo molecular pump in combination with a primary scroll pump was connected to the chamber inlet to achieve the required pressure. The chamber was connected to the end of one of the accelerator beamlines, see figure 4.2.
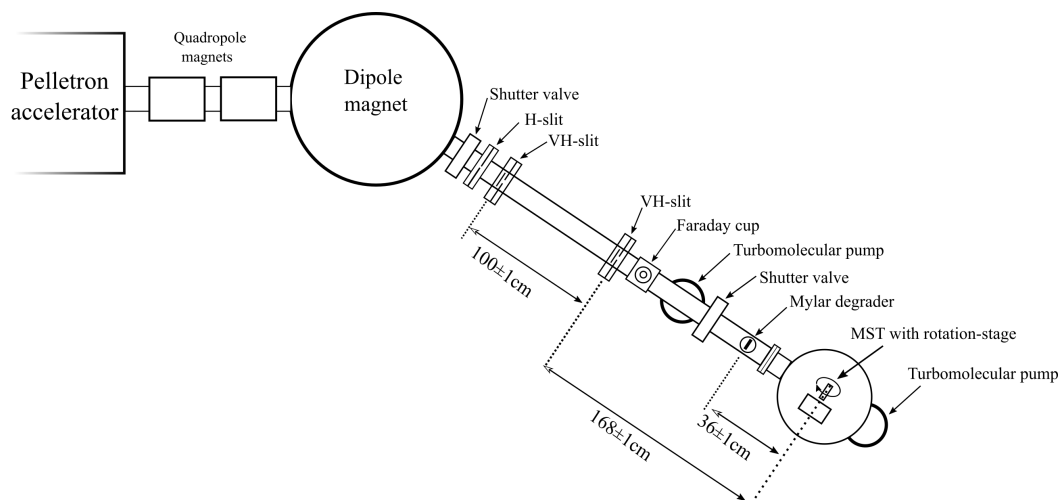

Figure 4.2: Schematic overview of beamline at Nishina center Pelletron accelerator (not to scale).

The positive ions accelerated by the Pelletron were filtered, steered and focused into the beamline using a set of quadropole magnets combined with a large dipole magnet. Proper adjustment of current in the two quadropole magnets and dipole magnet allow accurate selection of ion species of interest to the target down the beamline. A vacuum shutter separate the beamline from the main accelerator tube followed by two slits, one horizontal and another both vertical and horizontal (VH-slit). One meter down the beamline follows another VH-slit, these slits are used to define the beam diameter and decrease beam intensity. A Faraday cup collects the charge and is used to determine beam current and for optimizing accelerator focusing parameters. A second turbo-

Figure 4.3: A picture of the Pelletron beamline with target chamber setup.

molecular pump used for the beamline is placed near another shutter-valve separating the beamline from the target chamber. A mylar degrader was constructed with three layers of different thickness (0.5, 1, 1.5 µm) used to reduce beam energy, see figure 4.4a. The degrador position could be adjusted into the beam to change the beam energy.
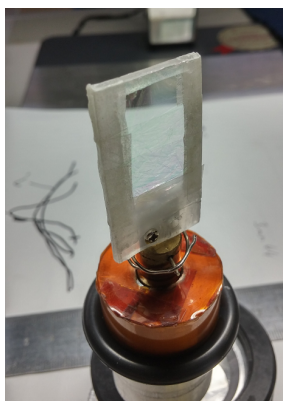
(a)

(b)

Figure 4.4: Figure (a) shows the constructed mylar degrador with varying mylar thickness. Figure (b) shows the rotation-stage with MST placed inside the target chamber.

The calibrated MST on the motorized rotation-stage was placed inside the chamber at the end of the beamline (see figure 4.4b). The alignment was done using a scintillator detector in order to determine the beam path. The rotation-stage was connected to a cable feedthrough that allowed angular control from outside the chamber using a computer controller.

4.2.1 Noise-sensitivity and precautions

To ensure optimal detector conditions proper precautions were taken to assure a noise free environment. The chamber was electrically insulated from the main accelerator beamline using a ceramic insulating washer in combination with a separate ground. As previously the preamplifiers were screwed tight on to the vacuum chamber and aluminium foil was used to protect the cable terminals. During detector operation the turbo pump directly connected to the target chamber as seen in figure 4.3 was turned off. Vibrations and electrical noise from the turbo pump caused significant detector noise and it was therefore necessary to maintain the vacuum using the beamline turbo pump. One significant contribution to the noise was the bias voltage supplies. Ripple currents from the switching power supply caused problems, accurate low ripple DC power supplies were therefore used. The output was connected to ferrite cores and a constructed low pass RLC low-pass filter circuit reducing high frequency signal noise further helped improve the signal to noise ratio. Due to the improved signal to noise ratio in the new arrangement a slight modification of the preamplifier circuit was made where the feedback capacitance was decreased to 1 pF with an increased resistance of 200 MOhm set for both E and dE detectors.

4.3 Ion beam selection

Four ions of different mass and charge state were selected for the experiment:

- 4 MeV $^{11}\text{B}^{3+}$

- 7 MeV $^{197}\text{Au}^{6+}$

- 25.5 MeV $^{197}\text{Au}^{16+}$

- 9 MeV $^{63,65}\text{Cu}^{5+}$

Ion range and energy loss in silicon were calculated for the chosen ions using SRIM simulations, see figure 4.5. Essential for our understanding of the detector performance for studying the $^{8}\text{Li}(\alpha, n)^{11}\text{B}$ reaction is the detection of ^{11}B. A selected ion species of $^{11}\text{B}^{3+}$ ions accelerated to 4 MeV using the Pelletron would be used at the beamline. The simulations of 4 MeV ^{11}B into silicon can be seen figure 4.5a which estimate a range of 5 μm into the silicon. This range would be sufficient to penetrate into the E detector in the MST, passing both dead-layers and dE detector. The amount of channeling of this ion is of particular interest for this work as well as the energy loss in both dead-layers.

In order to determine the thickness of the first dead-layer an ion with short range was selected which would stop in the dE detector without entering the second dead-layer. $^{197}\text{Au}^{6+}$ accelerated to 7 MeV was chosen mainly for this purpose. Simulation (see figure 4.5b) show a range below 2 μm into the silicon with substantial nuclear recoils due to the large mass of the gold ion, this range would not suffice to enter the E detector. A different charge species was selected with a charge state of $^{197}\text{Au}^{16+}$ reaching 25.5 MeV with large stopping power and range as seen in figure 4.5c. Particle identification of heavy nuclear fragmentation in nuclear transmutation experiments has been suggested as a possible use for the MST. These experiments will provide insight in the signal characteristics for the detection of heavy ions with large stopping power.

Finally, 9 MeV $^{63,65}Cu^{5+}$ with an intermediate stopping power with a range similar to Boron was selected (see figure 4.5d). The incentive for using this ion was to study both the channeling effect and compare signal characteristics with the other ions.
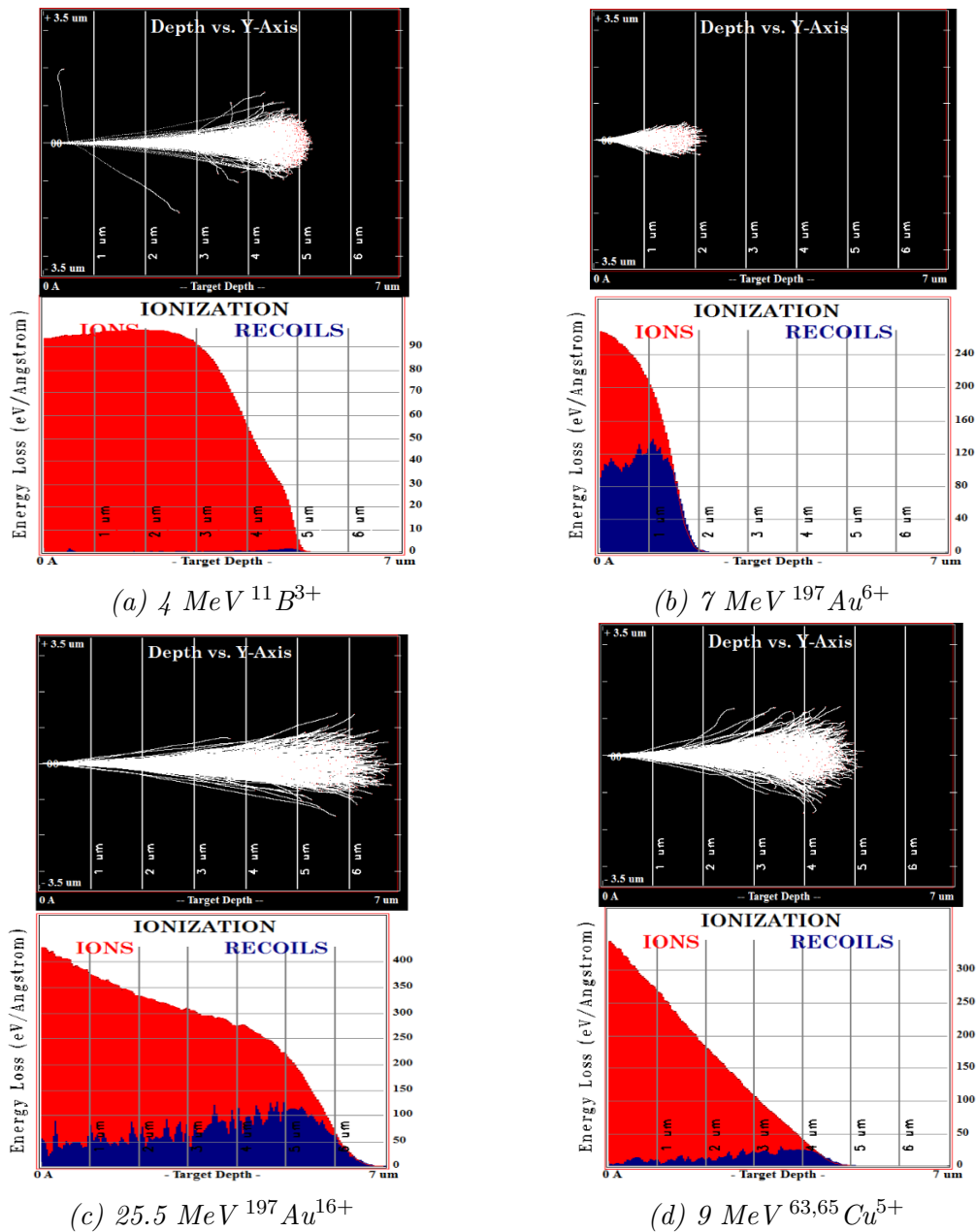

(a) 4 MeV $^{11}B^{3+}$

(b) 7 MeV $^{197}Au^{6+}$

(c) 25.5 MeV $^{197}Au^{16+}$

(d) 9 MeV $^{63,65}Cu^{5+}$

Figure 4.5: SRIM simulations of the ions selected for use in the Pelletron experiment. The ionizing energy loss from direct ion interaction and recoils have been calculated for the different ions.

4.4 Data acquisition setup

Since the previous DAQ computer setup used for testing the detector was no longer available a different DAQ setup had to be used at the Pelletron facility. The setup described in chapter 3.1 was modified to no longer require the external trigger using analog amplifier and discriminator. Instead, the DAQ was operating in a non-waveform mode using CAEN: DPP-PHA (digital pulse processing- pulse height analysis) firmware which both captures and processes the triggered pulses. DPP-PHA is necessary to reduce the large quantity of data using a fully digital approach capturing only the quantities of interest instead of full pulse traces, a block diagram of the process is seen in figure 4.6. The digital pulse traces after the decimator from all connected channels are passed through a trigger-timing filter and a trapezoid filter to extract the energy and time. The trigger-timing filter is used to generate a trigger and derive the time-stamp by using a RC-CR^2 algorithm. The RC filter or mean filter was used in the previous section to reduce high frequency noise in the pulse trace and CR^2 is the second order derivative of the trace which transforms the pulse into a bipolar with a zero crossing used to determine the time-stamp.
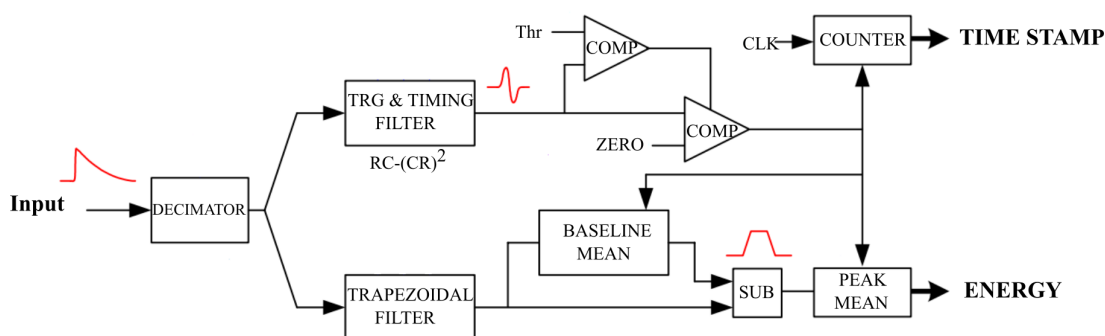

Figure 4.6: Block diagram of the digital pulse processing used to extract information from pulse traces[20].

In parallel with the trigger-timing filter the pulse trace is processed by a trapezoid filter transforming the charge-integrated and long exponential decay of the preamplifier output into a trapezoidal shape whose amplitude is proportional to the energy. A more detailed description of this process can be found in the reference [20].

Both time-stamp and energy is obtained from each of the 6 detector channels with a corresponding id 1-6. A coincidence trigger margin is set manually by observing the time difference between triggers in the dE and E detector. All events occurring within this margin adds to the particle multiplicity which is saved for each event. This can be used to determine dE-E coincidence events in case a particle interacts with more than one detector. Thus every event correspond to a vector with detector id, energy, time-stamp and multiplicity.

Chapter 5

Method and data processing

This chapter presents the method used for investigating the signal characteristics at different angles of incidence at the Pelletron beamline. Furthermore, the offline data analysis used to to filter and extract relevant information from the acquired data is discussed.

5.1 Method

Initial detector and setup optimization was performed using an ion beam of 4 MeV ^{11}B. The beamline slits were gradually opened while observing the preamplier output using an oscilloscope with the detector adjusted to zero degrees angle of incidence. In order to prevent radiation damage the slits were adjusted to reduce the count rate below 50 Hz in the dE3 detector. Data was collected for approximately 15 minutes for different bias voltages ranging from 0-100 for the E detector and and 0-7 volts for the dE detectors. This was done in order to determine the bias voltage yielding optimal detector resolution. When optimal bias voltage had been determined experiments were performed using the four selected ion beams. Initially, data was collected from 4 MeV ^{11}B with incrementally changing the detector angle in steps of 2.5 degrees from 0 up to 52.5 degrees collecting approximately 30000 events per angular setting with maximum 50 Hz per channel. This was followed by another set of measurements in increments of 1 degree from 0-15 degrees. The mylar degrador was used to investigate the detector response at different ion energies. he accelerator was configured for 7 MeV ^{197}Au ions and data was acquired at angles ranging from 0-60 degrees in steps of 5 to 10 degrees. The main intention for these experiments were to determine the first dead-layer thickness. The charge species was later changed to 25.5 MeV ^{197}Au^{16+} and experiments performed between 0-50 degrees in steps of 10 degrees. Finally, 9 MeV ^{63,65}Cu ions were used at the beamline. Experiments were performed from 0-15 in 0.5 degree increments in order to further investigate the channeling effect.

5.2 Digital data processing

The MST signal after the preamplifier from the 4 MeV ^{11}B was observed using an oscilloscope triggering on the E detector. A sample coincidence event in dE3 and E can be seen in figure 5.1a. In pursuance of the digitization of the data using the

DAQ the data acquisition settings were configured using MC^2Analyzer (MC^2A) software which allows full control over all the relevant DPP-PHA parameters for each acquisition channel such as trigger threshold, shaping parameters, etc [26]. While the shaping time was set for optimal detector resolution the coincidence timing-trigger threshold could be determined by observing the time difference between dE and E events in a timing histogram (figure 5.1). The timing-trigger filter was set to accept events in between 0 to 1.1 us based on these observations.

| (a) | (b) |
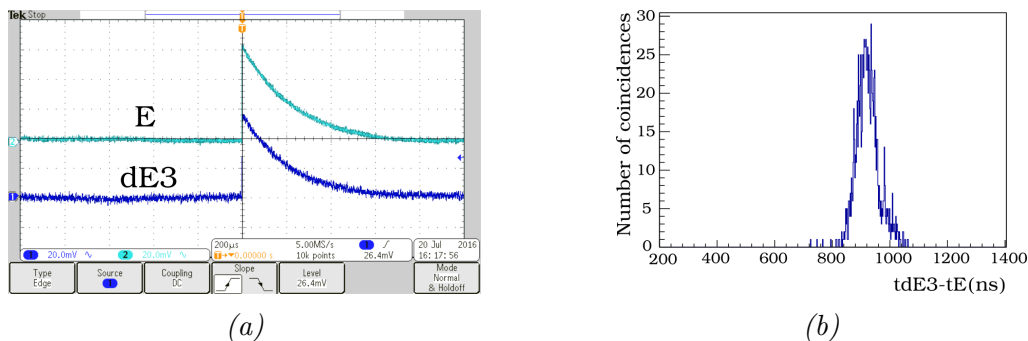
Figure 5.1: Figure (a) display one coincidence event of 4 MeV ^{11}B observed using an oscilloscope while (b) shows a histogram of the time difference between events in dE and E detectors.

The data acquired using DPP-PHA from the DAQ was analyzed using ROOT CERN software[22] which is a C++ based data analysis framework capable of handling large data analysis. Histogram data from all detector channels can be seen in figure 5.2 corresponding to 15 min of beam exposure. The beam was mainly directed to the dE3 detector, however, due to scattering events and undefined beam-halo as well as other beam impurities, events are seen in adjacent detector pads.
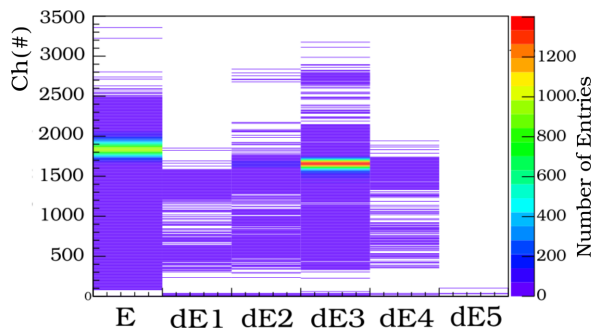

Figure 5.2: Unfiltered histogram data in all detector channels from 4 MeV ^{11}B.

In this work only one detector pad (dE3) is investigated since only this pad had been calibrated along the axis of rotation. The signal was therefore filtered to only include coincidence events in dE3 and the E detector, in figure 5.3a only coincidence events interacting with both dE3 and E are seen. However, some ions hitting the sides of the detector will also deposit some of their energy in the nearby detectors dE2 and dE4. By adding a constrained multiplicity of nhit=2 unwanted events are removed thus only ions passing through the dE3 and E detector are selected (figure 5.3). For convenience, dE3 is named dE in the coming sections.

The histograms of both dE and E after filtering are displayed in 5.4 with fitted Gaussian functions.
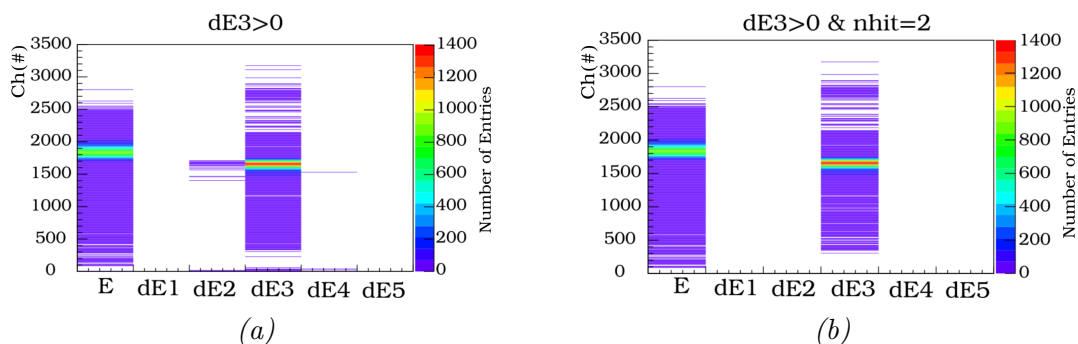
Figure 5.3: Figure (a) displays the coincidences in both dE3 and E, (b) displays the filtered data with added multiplicity constraint.
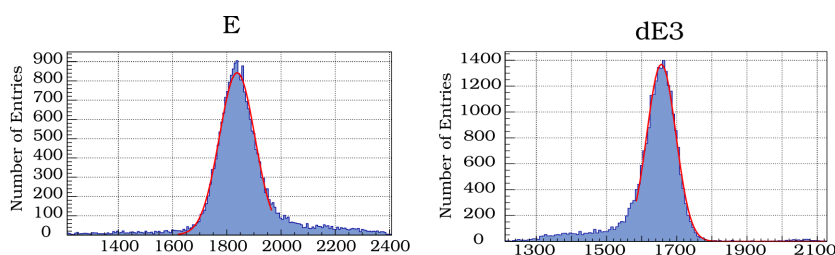

Figure 5.4: Histogram of 4 MeV ^{11}B in dE3 and E after filtering.

A 2D dE-E particle identification spectra for ^{11}B could be created with the coincidence data after filtering (figure 5.5).
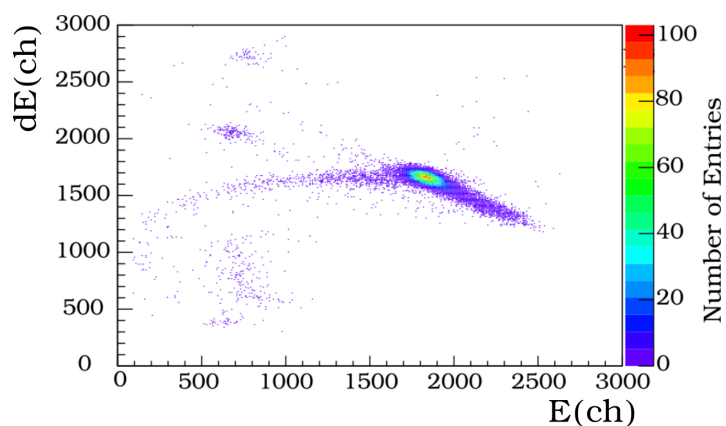

Figure 5.5: dE-E particle identification spectra for 4 MeV ^{11}B.

This spectra shows the main peak corresponding to the 4 MeV ^{11}B captured at 0 degrees angle of incidence. Furthermore, a tail extend towards lower energies starting from the main peak combined with a few other spots corresponding to other ion species and impurities in the ion beam. Interestingly, another tail extends towards higher energies starting from the main peak. This was the first observation of the channeling effect in the MST which is investigated in the following chapter.

Chapter 6

Results and discussion

In this chapter the results from the Pelletron experiment are presented and discussed. Firstly, the bias voltage yielding optimal resolution for both dE and E detector is conferred. Secondly, a general method used to quantify the channeling effect is presented and used to determine the channeling of ^{11}B and ^{63,65}Cu ions in the MST for varying angles of incidence. The influence of the channeling effect in the MST is discussed combined with suggestions for the optimal detector orientation. This analysis is proceeded by the investigation of both dead-layer thicknesses using data from ^{11}B combined with 7 MeV ^{197}Au. Based on the determined dead-layer thicknesses the detector is simulated in SRIM and in doing so verifying the accuracy of simulation by comparing with obtained results. Finally, the investigation is concluded with suggestions regarding optimal detector configuration and a discussion regarding limitations for particle identification using the MST.

6.1   Resolution vs bias voltage

To establish optimal working conditions for the MST prior to the angular experiments the bias voltage yielding best possible energy resolution needed to be defined. The detector was initially exposed to 4 MeV ^{11}B beam at 0 degree angle of incidence while varying dE and E detector bias voltage. The main peak in the spectra for both detectors were fitted with Gaussian functions as seen in figure 5.4 providing both FWHM and centroid peak position required to determine the detector resolution. Assuming linear correlation between the channel number and energy, the resolution for both detectors could be determined (see figure 6.1). Two data sets were gathered for both detectors at different times. A slight difference in resolution between the data sets can be attributed to a varying sensor temperature between the two experiments. The dE detector resolution improved with applied bias, stabilizing above 5 V at 6% expected from the increased charge collection due to the increasing depletion region. To prevent damaging the dE detectors a bias voltage of maximum 7 V was selected. In contrary, the E detector resolution indicated a deteriorating resolution with increased bias voltage with an optimal resolution at around 0 V of 7%. This unexpected behavior demonstrate that the depletion region increases inwards from the dE detector with increasing bias voltage. Since the ^{11}B has a short range into the E detector the built-in potential create a sufficiently large depletion region capable of capturing the charge generated
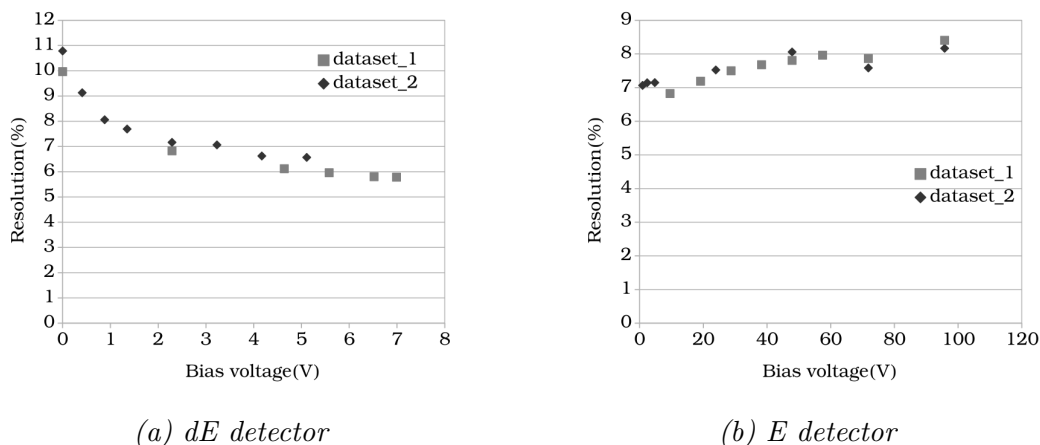
(a) dE detector

(b) E detector

Figure 6.1: Detector resolution vs bias for both detectors. The bias for dE was finally set to 7 V while 50 V for the E detector.

by the ion. The decreased resolution could be caused by increased electrical noise from bias power supply at greater current draw for higher bias voltages, this remains to be verified. A bias voltage of 50 V was set for the experiment as additional measure to increase the electric field to reduce plasma effects for heavier ions.

6.2 The channeling effect in the MST

6.2.1 4 MeV ^{11}B

One of the main objectives of this work was to determine the influence of channeling effect in the MST. The first indication of channeling was observed in the dE-E spectrum where a tail could be seen smearing the peak towards the right with increasing E signal and decreasing dE signal. This tail was noticeably angular dependent as was noticed in the two scenarios in figure 6.2. Channeled particles deposit less energy in the ultra-thin dE detector resulting in a greater signal in the E detector. The distribution of partially channeled particles generate a tail starting from the main peak. Commonly for very thin absorbers the peak resemble a landau distribution (refer to [25] for more information) with a tail extending to higher energies, however, at dominant channeling angles the tail resemble a Gaussian distribution see gray area in figure 6.8.
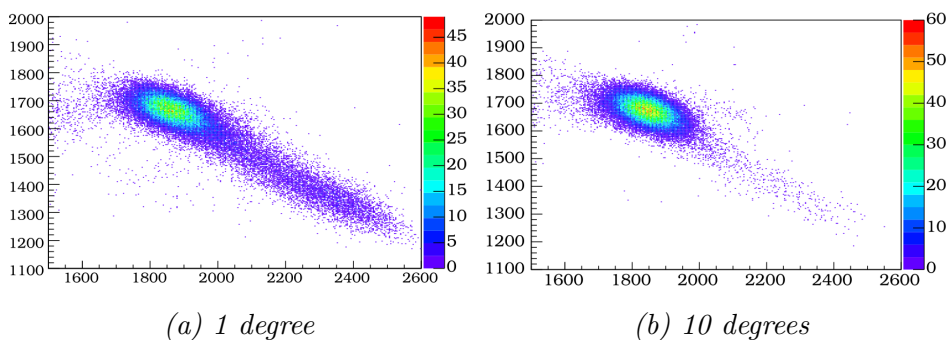

(a) 1 degree

(b) 10 degrees

Figure 6.2: 4 MeV Boron signal in MST at different angles.

In order to quantify the channeling effect a general definition is needed. The channeling ratio was defined as the number of coincidence events with energy above 3 sigma of the main peak in the E detector over the number of events within the main peak (see figure 6.8).
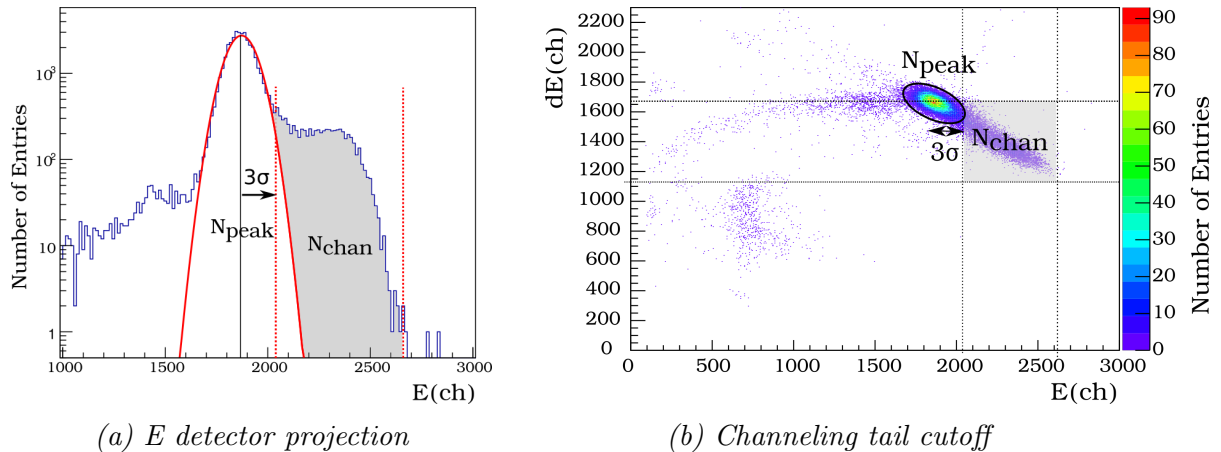

(a) E detector projection   (b) Channeling tail cutoff

Figure 6.3: These figures display the procedure used to define channeling ratio defined by the number of events in the channeling tail N_{chan} divided by the events in the main peak N_{peak}.

To further confine the channeling region the last bin in the tail with more than 2 counts is set as the limit for both dE and E to exclude any beam impurities with higher energy. This, in combination with a limiting dE cutoff at the centroid peak position, creates a box of channeled events used to determine the channeling ratio (see figure 6.3b). The uncertainty in the channeling ratio was determined from the uncertainty in the fit parameters of the Gaussian function in combination with Poisson statistics of the number of counts in the peak and channeling region. Using this algorithm the channeling ratio for 4 MeV ^{11}B could be determined at the different angles of incidence (see figure 6.4). Peaks with higher channeling ratio occur around 1, 20 and 37.5 degrees
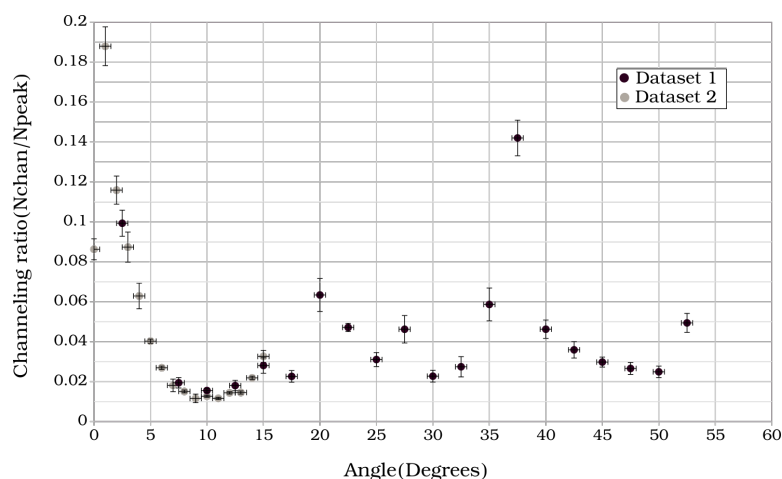

Figure 6.4: Channeling ratio as a function of detector angle θ (see figure 6.6b).

where the number of channeled particles are up to 19% for 1 degree angle of incidence. A clear minimum can be observed at around 10 degrees with less than 2% channeled

particles. VESTA[23] was used in order to determine the crystal orientation based on the observed peaks. A comparison between observed peaks and corresponding high symmetry crystal orientations is seen in figure 6.5. A suggested crystal orientation of
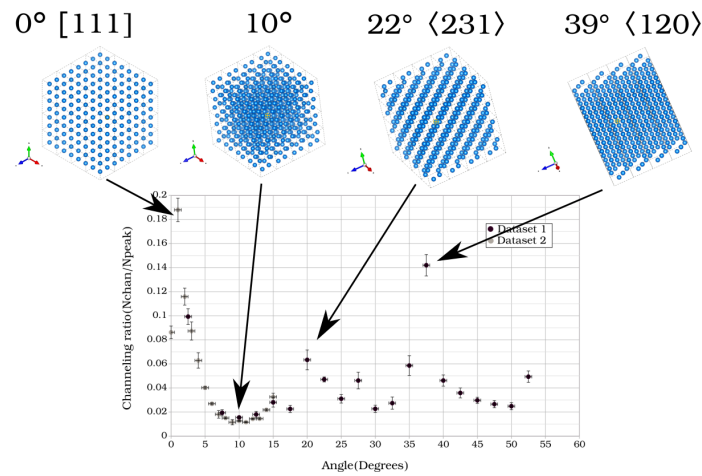

Figure 6.5: *Suggested crystal orientations for corresponding peaks with high channeling ratio.*

[111] correlates well with the obtained results, indicating peaks corresponding to $\langle 231 \rangle$[1] at 22 degrees and $\langle 120 \rangle$ around 39 degrees along the angle θ as can be seen in the Kikuchi pattern, see figure 6.6. The slight angular offset could have been caused by the cabling interfering with the rotation or in-proper positioning in target chamber. Since only angle θ has been investigated a mirror symmetry is left unbroken. The complete crystal orientation can be determined with further analysis along the detector angle ϕ, see figure 6.6b. It is however expected that this angle suffers from a greater amount of channeling since it follows a dominant crystal plane and should therefore be avoided. For optimal working conditions the detector should be angled $\theta = 10$ degrees with respect to the ion beam at the anisotripic orientation in between [111] and $\langle 231 \rangle$.
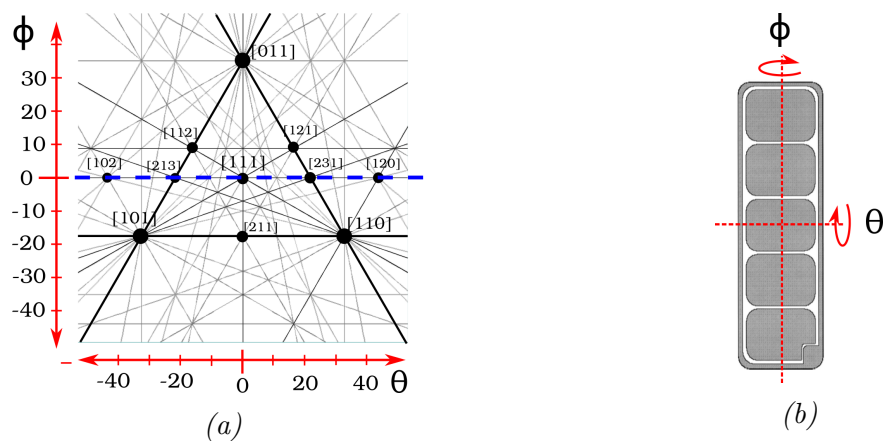

Figure 6.6: *The Kikuchi patten for silicon at [111] direction with indicated symmetries is seen in (a). The blue line indicates two possible orientations from [111] investigated in this experiment. Figure (b) shows the detector with corresponding rotation axis and angles.*

[1]This notation indicates the family of directions [123],[213],[231]...

Additionally, the length of the channeling tail was investigated for the main channeling peaks. The tail length for the channeling tail at 1 degree correspond to about 600 E channels which is approximately 35% of the peak position. This can be compared to the E detector resolution of 7%. The channeling tail at 37.5 degrees had a length of 1100 E channels correspond to approximately 50 % of the peak position. The longer tail at greater angles of incidence correspond to the longer crystal channel which allows for a much lower energy loss compared to respective unchanneled particle. This indicates the significance of the channeling effect in ultra-thin silicon detectors.

6.2.2   9 MeV ^{63,65}Cu

The channeling effect was also observed using 9 MeV ^{63,65}Cu ions as seen in figure 6.7a. The increased smear observed in the spectrum could be caused by the existence of the two naturally occurring isotopes of Copper 63 and 65. However, similarly to experiments using ^{11}B maximum channeling ratio occur near 1 degree with minimum channeling at around 10 degrees. The channeling peak is much wider in comparison ^{11}B as can be seen in figure 6.7b which is expected according to equation 2.2.5 predicting a large critical angle of 19 degrees for 9 MeV ^{63}Cu. This can be compared to the approximate FWHM of the peak which was 11 degrees. The model seem to fails at predicting the critical angle for heavy slow ions. On the other hand the critical angle for the channeling of 4 MeV ^{11}B was calculated to 5.5 degrees, this value can be compared to the peak at 1 degrees which has an approximate width of around 5 degrees. The channeling ratio for the copper data is above 10 degrees is inaccurate. At these greater angles of incidence the main peak is close to the second dead-layer which results in false channeling ratio due to lower number of counts in the main peak.
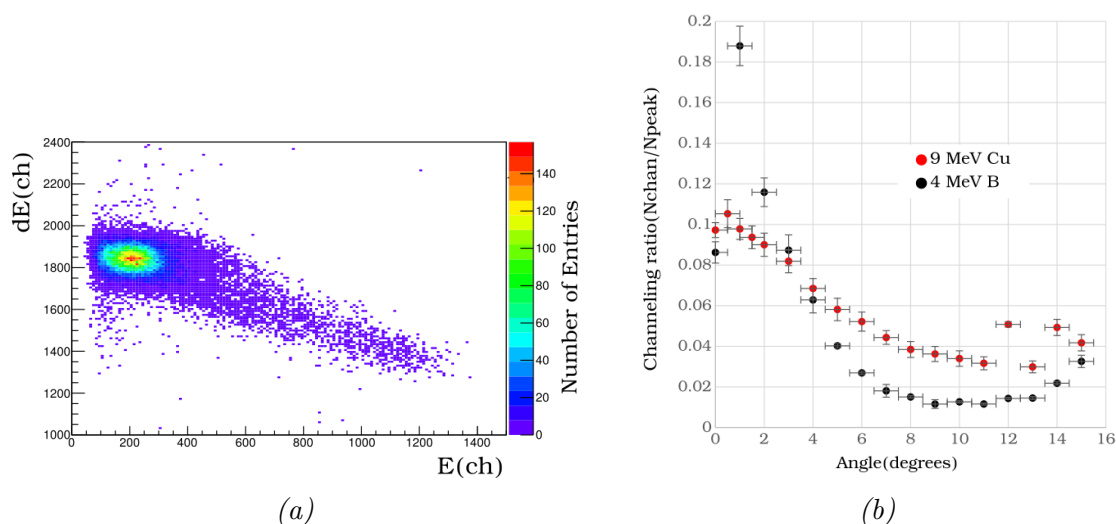

(a) *(b)*

Figure 6.7: Figure (a) shows the signal from 9 MeV ^{63,65}Cu at 0.5 degree angle of incidence. Figure (b) displays the channeling ratio with respect to angle for both 9 MeV ^{63,65}Cu and 4 MeV ^{11}B.

6.3   Detector dead-layers

Essential for the understanding of particle identification using the MST is the determination of the detector dead-layers. There are two dead-layers in the MST contributing to particle energy loss, one in front of the dE detector and a second in between the dE and E detector. In this section both dead-layers are determined using the data acquired at varying angles of incidence using 7 MeV ^{197}Au and 4 MeV ^{11}B.

6.3.1   First dead-layer

The 7 MeV ^{197}Au ion beam was chosen for its short range stopping in the dE detector allowing accurate identification of the first dead-layer thickness. In the analysis of the 7 MeV ^{197}Au only ions with multiplicity of 1 were selected, meaning particles which only deposit energy in the first dE detector without reaching the E detector. The histogram data of 7 MeV ^{197}Au can be seen in figure 6.8a with a fitted Gaussian displaying its centroid position x_{dE}. Two peaks were observed in the histogram, the peak with lower energy was likely caused by impurities in the accelerator beam and was not studied.
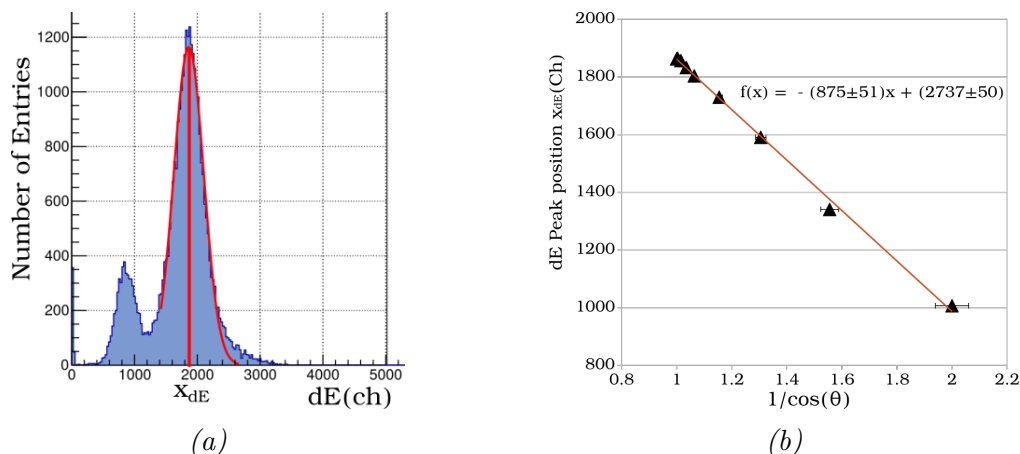

(a)   (b)

Figure 6.8: Figure (a) displays the 7 MeV ^{197}Au histogram data with a fitted Gaussian for 0 degree angle of incidence. The peak position at varying angle was used to determine the plot seen in figure (b).

In section 2.2.2 a method for determining the dead-layer thickness was presented which predicted the following linear relation,

$$x_{dE} = -\frac{E_{dl1}}{G_{dE}}\left(\frac{1}{\cos(\theta)}\right) + \frac{E_{tot}}{G_{dE}}$$

The centroid peak position x_{dE} was plotted with respect to $1/\cos(\theta)$ as seen in figure 6.10b. Since the energy of the incoming ion is known both the effective detector gain G_{dE} and energy lost in the dead-layer E_{dl1} could be calculated from the coefficients of the fitted function. Since $\frac{E_{tot}}{G_{dE}} = 2737 \pm 50$ the gain could be calculated to $G_{dE} = 2.56 \pm 0.05$ yielding $E_{dl1} = 2.25 \pm 0.14$ MeV lost in the dead-layer at zero degree angle of incidence. Using SRIM simulations the first dead-layer could be determined to 520 ± 25 nm of equivalent silicon thickness (see figure 6.9). The large stopping power of the 7 MeV ^{197}Au ion is of concern which could result in plasma effects as well as non-ionizing

energy losses through phonon excitations which affects the calculated gain. However, this calculation assume equal non-ionizing energy losses in both detector and dead-layer, with this approximation the gain does not affect the calculated dead-layer thickness.
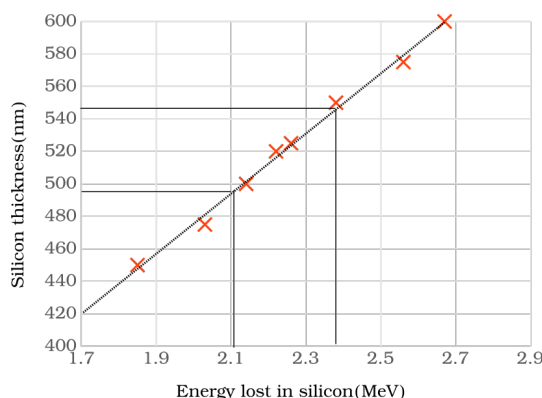

Figure 6.9: Simulated range of ^{197}Au in silicon at varying energy. The calculated ^{197}Au energy is indicated with corresponding range in silicon.

6.3.2 Second dead-layer

Combined with the previously determined first dead-layer thickness the second dead-layer thickness can be deduced using the data obtained from the 4 MeV ^{11}B run. Since the energy loss is roughly constant to a depth of 3 µm in silicon according to simulations (fig 4.5a) both dead-layers can be approximated as a single larger dead-layer where $E_{dl1} + E_{dl2} = E_{dl}$. Analogous to the calculation done in section 2.2.2 the signal in both detectors with respect to angle is given by $E_{tot} = G_{dE}x_{dE} + G_E x_E + \frac{E_{dl}}{\cos(\theta)}$ where $G_E x_E$ is the gain and signal of the E detector. This function can be rewritten accordingly,

$$(p_0 x_E - x_{dE}) = \frac{E_{dl}}{G_{dE}}\left(\frac{1}{\cos(\theta)}\right) - \frac{E_{tot}}{G_{dE}} \tag{6.3.1}$$

where,

$$\frac{\partial x_{dE}}{\partial x_E} = -\frac{G_{dE}}{G_E} = p_0. \tag{6.3.2}$$

Since the gain G_{dE} obtained using 7 MeV ^{197}Au was not trusted due to the vastly different stopping power the gain of both detectors were required. Luckily, the channeling effect provide the information needed. Based on energy conservation particles channeling through the first detector will deposit this energy in the second detector. The slope of the channeling tail therefore gives an insight in the gain ratio between the two detectors. Values for x_{dE} and x_E were obtained from the main peak coordinates while the gain ratio p_0 (see eqn. 6.3.2) was determined from the slope of linear fit of the channeling tail (see figure 6.10a). The average value for the gain ratio was determined to $p_0 = G_E/G_{dE} = 0.70 \pm 0.03$ while the peak position for dE and E were obtained at the different angles of incidence. In figure 6.10 the gain ratio and peak position have been plotted with respect to $1/\cos(\theta)$ which indicate a linear trend predicted by equation 6.3.2. The coefficients from the linear fit combined with determined gain ratio yield $G_{dE} = 0.94 \pm 0.02$ and $G_E = 0.66 \pm 0.05$. The significantly different gain for
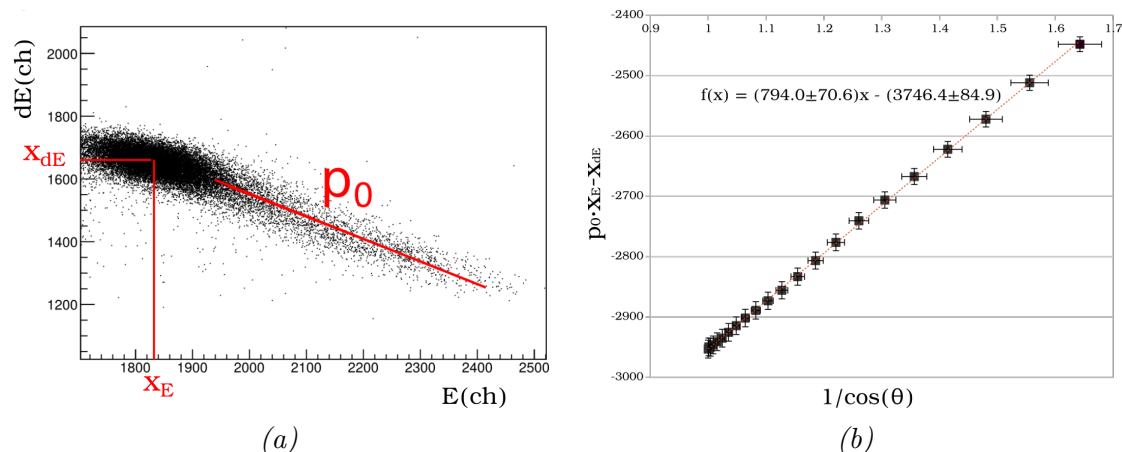
Figure 6.10: The 2D histogram in (a) displays the dE-E identification spectrum with centroid peak position and the slope of the channeling tail p_0 determined at varying angles of incidence to create the plot in (b).

dE detector compared to the previously determined gain of $G_{dE} = 2.56 \pm 0.05$ confirm the suspicions. Detailed calculations with full damage cascades performed in SRIM reveal an effective gain for 7 MeV ^{197}Au, excluding phonon and target damage losses, of $G_{dE} = 2.08 \pm 0.05$. The remaining difference in dE detector gain between the ^{197}Au and ^{11}B experiments indicate insufficient charge collection for heavy ions likely caused by the plasma effect. This observation could hinder the possible use of the MST in heavy ion identification applications.

Using the determined gain and coefficients from the linear fit, the energy lost in the dead-layers could be obtained. Combined with the known first dead-layer thickness additional simulations reveal the energy lost in the second dead-layer $E_{dl2} = 738 \pm 66$ keV. Similarly to the previous dead-layer calculation the second dead-layer thickness could be deduced to 788 ± 70 nm of equivalent silicon thickness.

6.3.3   Active dE detector region

With both dead-layers determined the size of the active dE detector region remain largely unknown. In order to determine the MST structure at the selected bias the detector was simulated in SRIM with a variable dE detector thickness (see simulation in appendix B). Simulations were performed at varying angles of incidence using 4 MeV ^{11}B on the simulated telescope. The energy deposited in the dE and E detector were calculated for different angles and compared to the experimentally obtained values (figure 6.11). At zero angle of incidence the thickness of the active dE detector region correspond to a thickness of 1.6 µm silicon. However, experimental data diverges from the simulated at greater angles of incidence and at 50 degrees the thickness correspond to approximately 1.3 µm silicon. This can be attributed to the assumption that the depletion region can be replicated using a step function. A more realistic scenario is a continuous depletion region where the electric field decreases at the boundaries of the active detector regions.
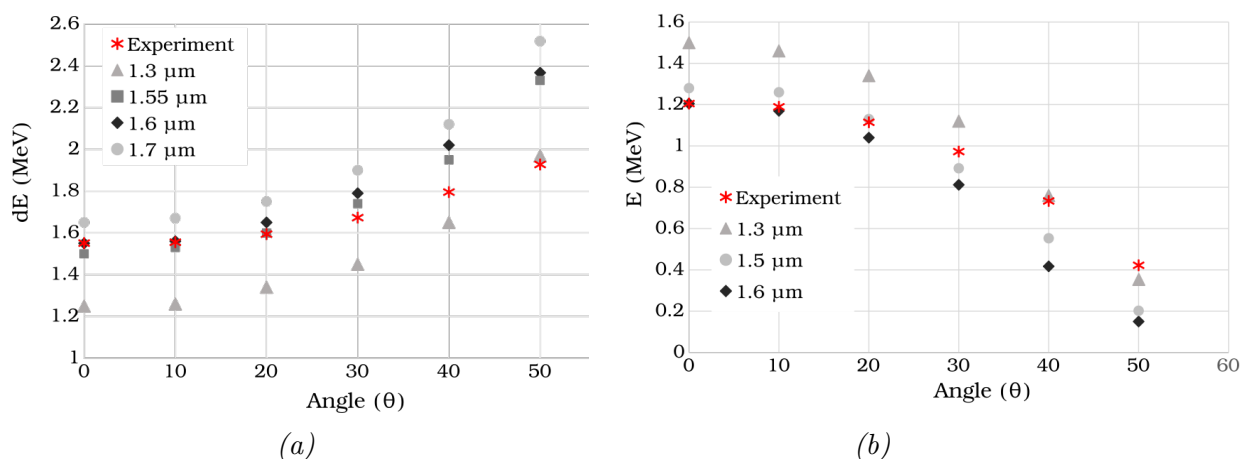
Figure 6.11: Simulated MST signal in the dE detector (a) and E detector (b) at different angles of incidence compared to calibrated experimental data.

6.3.4 Detector gain and calibration

Experiments were performed using mylar degraders with different thickness in order to vary the energy of the ^{11}B beam. The resulting ^{11}B signal after the degraders of different thickness can be seen in figure 6.12 with the corresponding calculated beam energy using SRIM.
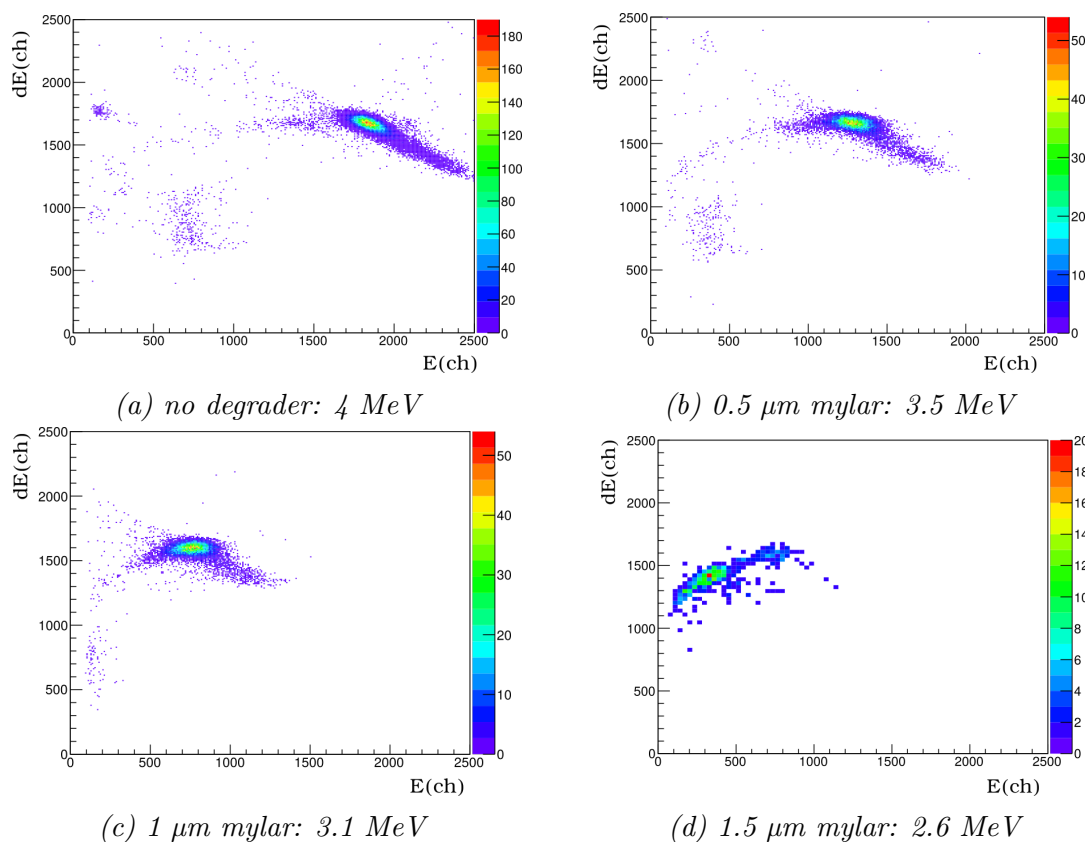

(a) no degrader: 4 MeV

(b) 0.5 µm mylar: 3.5 MeV

(c) 1 µm mylar: 3.1 MeV

(d) 1.5 µm mylar: 2.6 MeV

Figure 6.12: MST signal from ^{11}B at different energies.

The detector signal of the ^{11}B beam after degrader thickness with corresponding beam energy energies 4, 3.5, 3.1 and 2.6 MeV could be compared with the response from the replicated detector in the simulation program. ^{11}B ions at the different energies were simulated at zero degree angle of incidence into the detector with (520+1600+788) nm silicon corresponding to the first dead-layer, dE detector and the second dead-layer respectively. The transmitted ion energy corresponding to the energy deposited in the E detector could be compared to the calibrated signal from the MST of the ions at different energy, see figure 6.13.
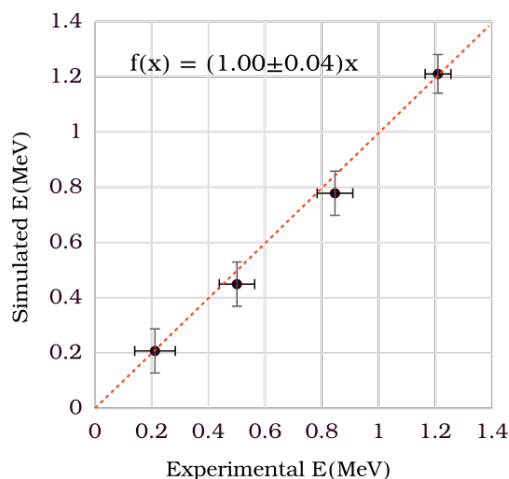

Figure 6.13: Simulated vs calibrated E detector response at varying ^{11}B energy.

The response from the E detector show that the calibration is indeed linear with respect to the simulated values. To further conclude the accuracy of the determined detector characteristics simulations could be evaluated using a second independent simulation program such as GEANT4 [27]. Since the dE-E identification spectra of ^{11}B is almost horizontal in the investigated energy regime the dE detector signal could not be compared due to the insufficient detector resolution.

6.3.5   25.5 MeV ^{197}Au

In addition to 7 MeV ^{197}Au a different charge state was tested with 25.5 MeV. Unfortunately due to large amount of impurities the beam species could not be properly identified.

6.3.6   Optimal detector configuration and outlook

This work provide significant information of the MST characteristics in an in-beam environment in preparation for the study of the ^{8}Li(^{4}He, n)^{11}B reaction cross-section. Both dead-layers and active dE detector region have been determined, combined with an extensive investigation revealing the influence of the channeling effect in the MST. To assure optimal detector performance with minimal channeling effect the telescopes should be oriented $\theta = 10$ degrees facing the anisotropic region indicated in the Kikuchi pattern, seen in figure 6.14a. Based on the determined dead-layer thicknesses the detector threshold for the detection of ^{11}B could be determined. The minimum detectable
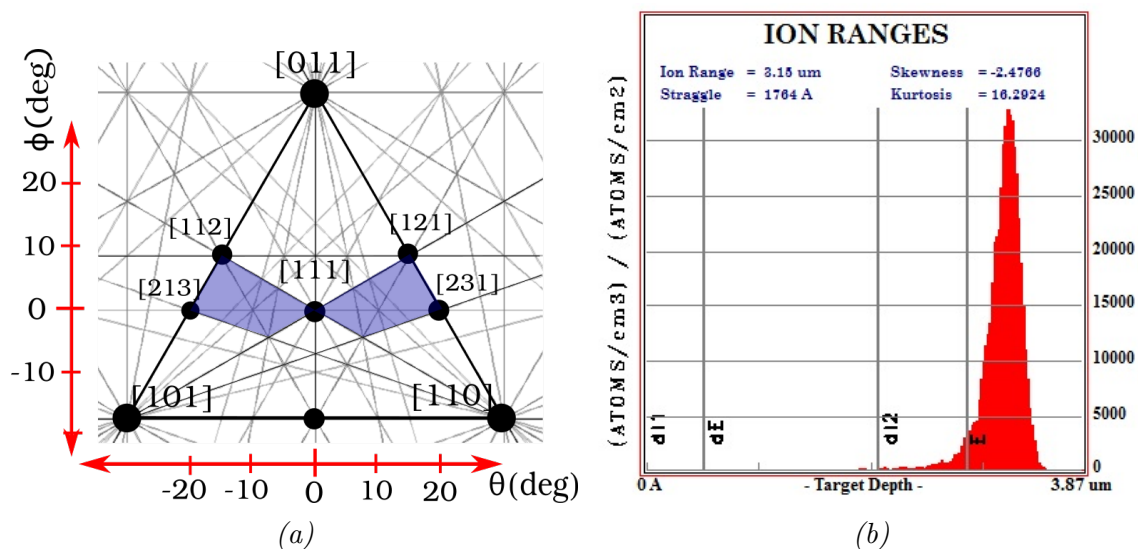
Figure 6.14: Kikuchi pattern of [111] silicon, the blue regions indicate optimal detector orientation with low particle channeling. The angles correspond to the detector orientations indicated in figure 6.6b. Figure (b) show the simulated range of 2.4 MeV [11]B into the detector at 10 degrees angle of incidence.

[11]B with the detector oriented 10 degrees was 2.4 MeV based on range simulations using a detector thickness of (520+1550+788) nm, see figure 6.14b.

Due to the limited beam-time only one detector pad was investigated in this work. Future experiments could reveal the similarity of the dead-layer thicknesses between detector pads on each MST which likely varies slightly due to discrepancies in the manufacturing process. Additional experiment could determine the channeling effect along ϕ, in doing so, verifying the exact crystal orientation of the MST.

6.4 Conclusion

This work is dedicated to detailed characteristics of the dE-E monolithic silicon telescope essential for the future use of the MST in the low energy cross-section measurement of $^{8}\text{Li}(^{4}\text{He, n})^{11}\text{B}$. Restricting the angle of incidence of particles to 10 degrees in between [111] and $\langle 231 \rangle$ would result in a significantly improved signal by reducing the channeling effect. In addition, the detector dead-layers could be determined to 520 ± 25 nm for the first and 788 ± 70 nm for the second of equivalent silicon thickness with an active dE detector region of 1.6 µm at zero degrees angle of incidence. Using the identified detector configuration the minimal ^{11}B energy at the optimal MST orientation of 10 degrees was determined to 2.4 MeV. Furthermore, experiments reveal possible limitations for heavy ion particle identification due to phonon losses and in particular plasma effects affecting the charge collection in the ultra-thin dE detector.

Appendices

Appendix A

The Tandem Pelletron accelerator

In this experiment a type of particle accelerator is used based on the the old principle of electrostatic acceleration of charged particles, called the Pelletron accelerator. Similar to Van Der Graaf accelerators the Pelletron achieve large electrostatic fields from a charge carrying belt. Unlike the Van de Graaf accelerator the belt is made out of a chain of insulated metallic pellets thereby its name 4. The Tandem Pelletron used in this experiment is of type 5SDH-2 developed by National Electrostatic Corp operating at Nishina center, RIKEN.
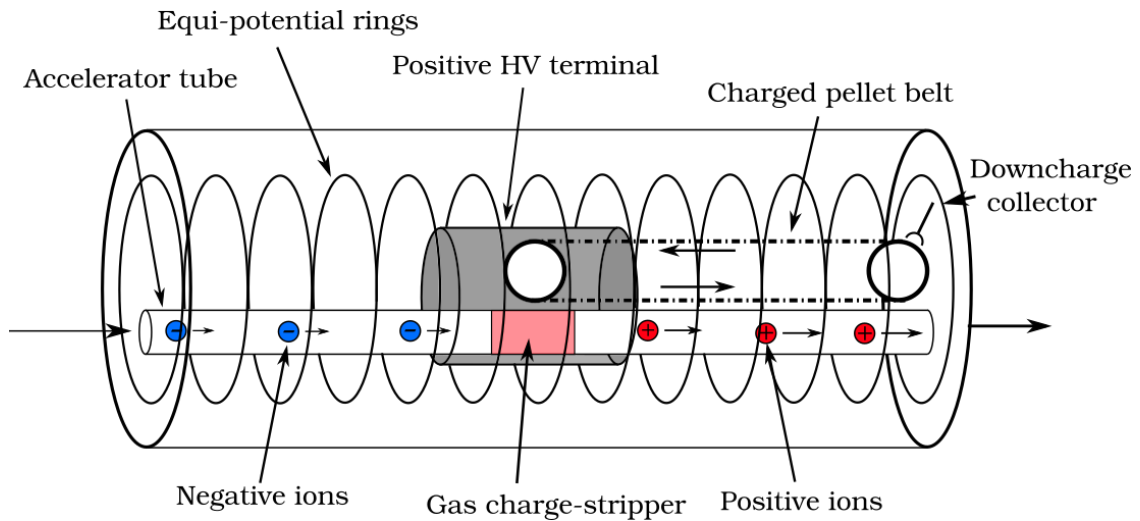

Figure A.1: Cross-section of a pelletron accelerator.

Negative ions are created in an ion gun at one end of the accelerator using a Source of Negative Ions by Cesium Sputtering (SNICS)[18]. The transfer of the valence electron from Cs to the sample of choice inserted in the ion gun generate negative ions of charge -1 which are accelerated out from the gun and steered into the Pelletron accelerator.

A schematic overview insides the Pelletron accelerator is seen in figure A.1. A large positive charge is accumulated at a terminal in the middle of the accelerator reaching potentials up to 1.7 MV. This high potential can be achieved without discharge by containing the accelerator inside a high pressure chamber with high density SF_6 gas. When negative ions are introduced at one end of the accelerator they will accelerate towards the positive high voltage terminal. when reaching the terminal a stripper gas

of Rubidium awaits the ions which will strip electrons away from the ions thereby changing the ion charge from negative to a variety of positive charge states. The charge conversion results in a repulsive force on the ions from the positive terminal, the ions will therefore accelerate once again away from the terminal towards the other end of the accelerator. This accelerator method allows makes it possible to reach greater ion energies with lower terminal voltage compared to single stage electrostatic accelerators. Depending on the charge state of the resulting ion after the charge stripper the ions will obtain a final energy E_{ion} at the end of the accelerator given by,

$$E_{ion} = V \cdot (n+1)$$

where n is the final charge state of the ion and V is the potential of the positive HV terminal. The final positive ion beam accelerated by the Pelletron contain many different charge states with different energy. The beam therefore require further charge and momentum selection which is done using a large dipole bending magnet combined with a set of focusing quadropole magnets which select and focuses the beam on to the target.
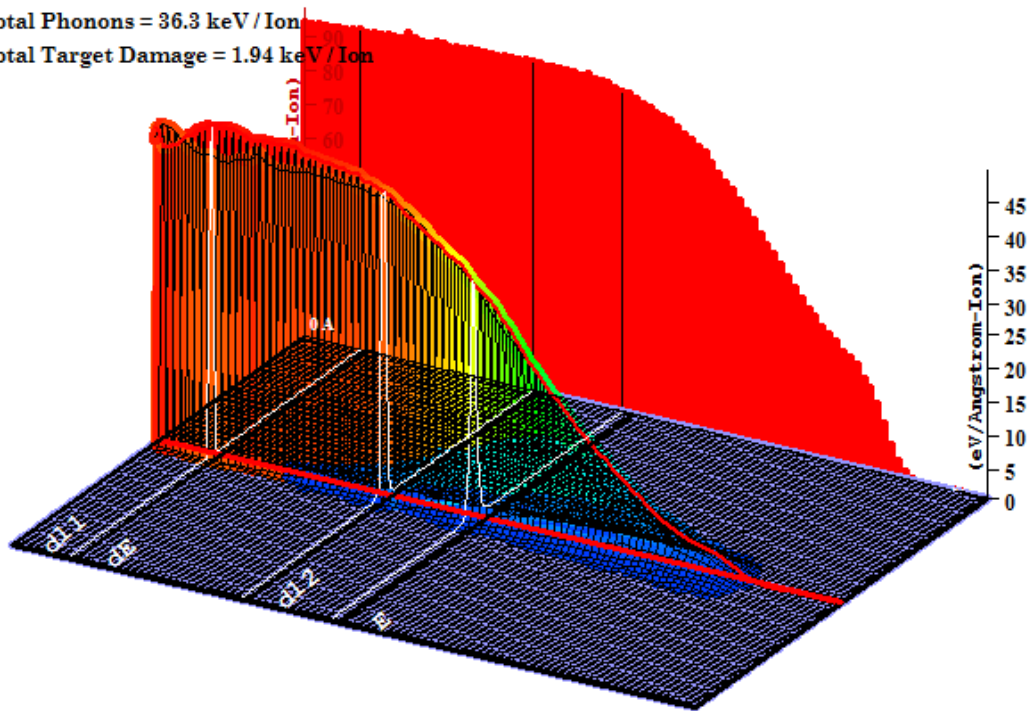
Appendix B

MST simulated in SRIM

Figure B.1: Ionization inside replicated MST structure in SRIM with 4 MeV ^{11}B beam.

Bibliography

[1] Oberhummer, Heinz, Attila Csoto, and Helmut Schlattl. "Bridging the mass gaps at A= 5 and A= 8 in nucleosynthesis." arXiv preprint nucl-th/0009046 (2000).

[2] Fields, Brian D., Paolo Molaro, and Subir Sarkar. "Big-bang nucleosynthesis." arXiv preprint arXiv:1412.1408 (2014).

[3] Kajino, Toshitaka, et al. "Fusion reactions in supernovae and the early universe." Progress of Theoretical Physics Supplement 154 (2004): 301-308.

[4] Kajino, Toshitaka. "Inhomogeneous big-bang model, revived, and evolution of the light elements in cosmic rays." Nuclear Physics A 588.1 (1995): c339-c343.

[5] La Cognata, M., et al. "On the magnitude of the 8 Li+ 4 He→ 11 B+ n reaction cross section at the Big-Bang temperature." Physics Letters B 664.3 (2008): 157-161.

[6] Terasawa, M., et al. "New Nuclear Reaction Flow during r-Process Nucleosynthesis in Supernovae: Critical Role of Light, Neutron-rich Nuclei." The Astrophysical Journal 562.1 (2001): 470.

[7] Kurata-Nishimura, M., et al. "A New approach for cross section measurements at low energies using a monolithic silicon telescope." Nuclear Physics A 758 (2005): 162-165.

[8] S. Nishimura, M. Kurata-Nishimura, "8Li(alpha,n)11B reaction measurement using monolithic silicon telescope" RIKEN Accel. Prog. Rep. 39 (2006).

[9] La Cognata, M., et al. "Toward correction-free 8Li (alpha, n) 11B data at the Gamow energy of explosive nucleosynthesis." Journal of Physics G: Nuclear and Particle Physics 37.10 (2010): 105105.

[10] Gemmell, Donald S. "Channeling and related effects in the motion of charged particles through crystals." Reviews of Modern Physics 46.1 (1974): 129.

[11] Knoll, Glenn F. Radiation detection and measurement. John Wiley & Sons, 2010.

[12] Amorini, Francesca, et al. "Monolithic silicon telescope as position sensitive detector." Nuclear Physics B-Proceedings Supplements 197.1 (2009): 194-197.

[13] Musumarra, A., et al. "Implanted silicon detector telescope: New developments." Nuclear Instruments and Methods in Physics Research Section A: Accelerators, Spectrometers, Detectors and Associated Equipment 409.1 (1998): 414-416.

[14] Williams, Raymond N., and Ewan M. Lawson. "The plasma effect in silicon semi-conductor radiation detectors." Nuclear Instruments and Methods 120.2 (1974): 261-268.

[15] `https://www.iso.org/obp/ui/#iso:std:42052:en` accessed 10/2016

[16] Kordyasz, A. J., and E. Kulczycka. "15. Double sided strip monolithic silicon E-dE telescope produced by Quasi-Selective Epitaxy." WARSAW, March 2008: 44.

[17] Herb, R. G. "The Pelletron Accelerator." IEEE Transactions on Nuclear Science 18.3 (1971): 71-75.

[18] Sala, O., et al. "Source of negative ions by cesium sputtering."

[19] Ziegler, James F., Matthias D. Ziegler, and Jochen P. Biersack. "SRIM–The stopping and range of ions in matter (2010)." Nuclear Instruments and Methods in Physics Research Section B: Beam Interactions with Materials and Atoms 268.11 (2010): 1818-1823.

[20] CAEN Nuclear physics: WP2081 Digital Pulse Processing in Nuclear Physics

[21] Huhtinen, Mika. "Simulation of non-ionising energy loss and defect formation in silicon." Nuclear Instruments and Methods in Physics Research Section A: Accelerators, Spectrometers, Detectors and Associated Equipment 491.1 (2002): 194-215.

[22] Brun, Rene, and Fons Rademakers. "ROOT—an object oriented data analysis framework." Nuclear Instruments and Methods in Physics Research Section A: Accelerators, Spectrometers, Detectors and Associated Equipment 389.1 (1997): 81-86.

[23] K. Momma and F. Izumi, "VESTA 3 for three-dimensional visualization of crystal, volumetric and morphology data," J. Appl. Crystallogr., 44, 1272-1276 (2011).

[24] Weber, S., Ch Schetelich, and V. Geist. "Computer-aided evaluation of kossel patterns obtained from quasicrystals." Crystal Research and Technology 29.5 (1994): 727-735.

[25] Leo, William R. Techniques for nuclear and particle physics experiments: a how-to approach. Springer Science and Business Media, 2012.

[26] `http://www.caen.it/csite/CaenProd.jsp?idmod=859&parent=38` accessed 12/2016

[27] Agostinelli, Sea, et al. "GEANT4—a simulation toolkit." Nuclear instruments and methods in physics research section A: Accelerators, Spectrometers, Detectors and Associated Equipment 506.3 (2003): 250-303.